Hysteresis of natural magnetite ensembles: Micromagnetics of silicate-hosted magnetite inclusions based on focused-ion-beam nanotomography

Even S. Nikolaisen[1], Richard Harrison[1,2], Karl Fabian[1], Suzanne A. McEnroe[1]

[1]Norwegian University of Science and Technology (NTNU), S. P. Andersens veg 15a, 7031 Trondheim, Norway
[2]Department of Earth Sciences, University of Cambridge, Downing Street, Cambridge CB2 3EQ, UK

Key Points:

- The 3D geometries of more than 400 silicate-hosted magnetite inclusions were measured using focused ion-beam nanotomography
- Micromagnetic modelling show that inclusions adopt multiple domain states, spanning the entire range of common domain-state diagnostic plots
- Geometric variability of naturally formed magnetite in silicate, explains scatter of magnetic parameters in the PSD region of the Day plot

Corresponding author: Even Nikolaisen, even.nikolaisen@ntnu.no

Abstract

Three-dimensional geometries of silicate-hosted magnetic inclusions from the Harcus intrusion, South Australia have been determined using focused-ion-beam nanotomography (FIB-nt). By developing an effective workflow, the geometries were reconstructed for magnetic particles in a plagioclase (162) and a pyroxene (282), respectively. For each inclusion, micromagnetic modelling using MERRILL provided averaged hysteresis loops and backfield remanence curves of 20 equidistributed field directions together with average M_s, M_{rs}, H_c, and H_{cr}. The micromagnetic structures within each silicate are single-domain, single-vortex, multi-vortex and multi-domain states. They have been analyzed using domain-state diagnostic plots, such as the Day plot and the Néel plot. SD particles can be subdivided into groups with dominant uniaxial anisotropy ($M_{rs}/M_s \sim 0.5$ and $10 < H_c < 100$ mT) and mixed uniaxial/multiaxial anisotropy ($M_{rs}/M_s \sim 0.7$ and $10 < H_c < 30$ mT). Most single-vortex particles lie on a trend with $0 < M_{rs}/M_s < 0.1$ and $0 < H_c < 10$ mT, while others display a broad range of intermediate M_{rs}/M_s and H_c values. Single-vortex and multi-vortex states do not plot on systematic grain-size trends. Instead, the multi-component mixture of domain states within each silicate spans the entire range of natural variability seen in bulk samples. This questions the interpretation of bulk average hysteresis parameters in terms of grain size alone. FIB-nt combined with large-scale micromagnetic simulations provides a more complete characterization of silicate-hosted carriers of stable magnetic remanence. This approach will improve the understanding of single-crystal paleomagnetism, and enable primary paleomagnetic data to be extracted from ancient rocks.

1 Introduction

A fundamental task in rock magnetism is to identify the magnetic domain states adopted by natural remanence carriers, because these control the remanence acquisition process, the stability of the remanent magnetization over geological time, and subsequently the reliability of the stored paleomagnetic information. Most rocks contain a mixture of magnetic minerals covering a broad range of particle sizes and shapes. Rock magnetism broadly classifies these particles into superparamagnetic (SP), stable single-domain (SD), pseudo-single-domain (PSD), and multi-domain (MD) states, with the boundaries between states originally based on experimental results [*McNab et al.*, 1968; *Dunlop*, 1973; *Dunlop and Bina*, 1977; *Soffel*, 1977]. Based on the magnetic material properties of magnetite, these observed boundaries could be related to theoretical calculations for regular particle geometries [*Butler and Banerjee*, 1975; *Argyle and Dunlop*, 1984; *Enkin and Dunlop*, 1987; *Enkin and Williams*, 1994], although the influence of shape has been recognized [*Stacey*, 1961; *Fabian and Hubert*, 1999; *Witt et al.*, 2005]. Theoretical values for the SP-SD and SD-PSD transition sizes agree very well with the experimentally determined boundaries of 0.025-0.030 μm and 0.050-0.084 μm for crushed and grown magnetite crystals. Experimental studies are limited to synthetic or natural particle ensembles with high variability in size and shape with the exception of a study on synthetic samples generated by lithography, where monocrystallinity could not be ensured [*Krása et al.*, 2009]. Magnetite particles directly above the upper SD limit assume an intermediate state in experimental and theoretical studies. Because they appear to be related to a stable and single-domain like experimental behavior, for which *Stacey* [1961] coined the notion of PSD remanence, they are commonly referred to as PSD particles. From a theoretical view such particles are intermediate between two characteristic length scales, the SD-limit of $\approx 7\ \lambda_{ex}$, where $\lambda_{ex} = \sqrt{2\,A/(\mu_0\,M_s^2)}$ is the exchange length, and the domain wall width of $\approx 5\ \sqrt{A/K_1}$. Here A denotes the exchange constant, K_1 the magnetocrystalline anisotropy constant, M_s the saturation magnetization, and μ_0 the vacuum permeability. For magnetite the intermediate size range lies roughly between 0.070 μm and 0.200-0.300 μm, however, the formation of clearly defined homogeneously magnetized domains does not occur below grain sizes of about 2 μm. *Nagy et al.* [2019] modelled grains up to the micron range and observed domain wall formation in unconstrained micromagnetic models. What is missing, is a comprehensive survey of magnetization states and predicted hysteresis prop-

erties for naturally occurring magnetite particles across, and beyond, the SD state. Here we develop a method to achieve such a survey based on FIB tomography combined with micromagnetic modeling.

To compare our model results to measurements on sized magnetite samples, we consider several isothermal measurements that have been developed to quantify the characteristic domain states of natural remanence carriers. The most common approach is based on the measurement of bulk average magnetic hysteresis parameters, such as saturation magnetisation M_s, saturation remanent magnetisation M_{rs}, coercivity H_c, and coercivity of remanence H_{cr}. Two intensely studied diagrams are the Day plot of M_{rs}/M_s versus H_{cr}/H_c [*Day et al.*, 1977], and the Néel plot of M_{rs}/M_s versus H_c [*Néel*, 1955], which are based on bulk hysteresis parameters that can be quickly and easily measured in most rock magnetic laboratories [*Dunlop*, 2002; *Tauxe et al.*, 2002]. It is well known that their interpretation is ambiguous without detailed knowledge of the underlying magnetic ensemble [*Roberts et al.*, 2018]. To relate domain state to geometrical measurements, the theoretical diagram of *Butler and Banerjee* [1975], and later revisions [*Fabian et al.*, 1996; *Muxworthy and Williams*, 2006], is commonly used to characterise the domain state of magnetic particles based on particle length and axial ratio. This approach assumes that magnetic particles can be effectively approximated as prolate ellipsoids.

Here we apply our workflow and method to magnetite particles within silicate-hosted magnetic inclusions. This setting is abundant and important for studying the Earth's magnetic field, magmatic evolution, geochemical interaction, stabilityand oxygen fugacity [*Feinberg et al.*, 2005; *Tarduno et al.*, 2020]. Magnetite is the most significant Fe-oxide for paleomagnetic studies, and magnetite i known to form as exsolved or included particles in silicates like plagioclase [*Davis and Letters*, 1981; *Feinberg et al.*, 2005; *Usui et al.*, 2015] and pyroxene [*Fleet et al.*, 1980; *Frandsen et al.*, 2004; *Renne et al.*, 2002; *Feinberg et al.*, 2004] within a wide range of geologic settings. *Davis and Letters* [1981] document that magnetite exsolves several micrometer long rods in 2-4 different directions in plagioclase from oceanic gabbros. The crystallographic relationship between magnetite needles and a plagioclase host was determined by [*Wenk et al.*, 2011]. They observed a single set of magnetite needles oriented parallel to the [001] axis of plagioclase, with the needle elongation direction corresponding to the [110] direction of magnetite and the (111) planes of magnetite oriented subparallel to (120) and ($\bar{1}$20) planes of plagioclase. Within pyroxene (CPX) iron oxide inclusions occur parallel to (010), where all inclusions are elongated and with the long axis subparallel to both [100] and [001] [*Renne et al.*, 2002; *Feinberg et al.*, 2004]. In orthopyroxene exsolved oxide lamellae are known from optical and transmission electron microscopy. Ilmenite lamellae are present as coherent rods and blades where (001) ilmenite is epitaxially intergrown on (100) pyroxene, and the a-axis of ilmenite is parallel to the c-axis of pyroxene [*McEnroe et al.*, 2004]. There the ilmenite contained hematite lamellae parallel to the (001) of the ilmenite. The incorporation of iron into the silicates is not confirmed, but suggested to occur at primary subsolidus mineral formation and exsolve magnetite well above its curie temperature [*Feinberg et al.*, 2004; *Fleet et al.*, 1980] for pyroxene. The exact process for exsolving magnetite in plagioclase is so far not established, but once the orientation relationship is established the phase boundary between plagioclase and magnetite can be established [*Wenk et al.*, 2011].

The advent of high-resolution focused-ion beam nanotomography (FIB-nt), combined with the development of powerful finite-element micromagnetic (FEM) software optimised for rock magnetic applications [*Ó Conbhuí et al.*, 2018; *Fabian and Shcherbakov*, 2018], provides a new opportunity to perform domain-state diagnosis from first principles. FIB-nt is performed on a dual-beam electron microscope that combines the high-resolution imaging capabilities of a field-emission gun scanning electron microscope (FEG-SEM) with the nm-precision slicing capabilities of a FIB [*Fagerland*, 2014; *Brogden*, 2015]. This technique is widely used to analyse biological samples [*Beckwith et al.*, 2015; *Guehrs et al.*, 2017; *Mulders et al.*, 2006], alloys [*Cao et al.*, 2009; *Ding and Jones*, 2011] and geological materials

[*Einsle et al.*, 2016; *ter Maat et al.*, 2020; *Warr et al.*, 2014; *Lascu et al.*, 2015]. The process is destructive, as the slicing destroys the prepared sample area. However, it has higher spatial resolution than comparable non-destructive methods of X-ray computed tomography, enabling the morphology of particles spanning the SD to MD range to be reconstructed in 3D. Rather than attempting to solve the inverse problem of unmixing domain states from a series of magnetic hysteresis measurements, the combined FIB-nt-FEM approach enables forward models of domain states and hysteresis properties to be calculated from direct 3D observations of a representative particle ensemble. Evaluating magnetic signatures in geologic samples will always be challenging. The complexities of particle size, shape, spacing, chemical composition, stoichiometry and stress will generate unique mineralogical settings, and it is a fair question raised by *Lascu et al.* [2015] whether domain-state diagnosis might be an unachievable ideal? Here we show that FIB-nt-FEM is able to resolve domain-state ambiguities associated with the size, shape and spacing of particles. In combination with other techniques, such as energy-dispersive X-ray spectroscopy (EDS) and high-resolution electron backscattered diffraction (HR-EBSD), it has the potential to resolve ambiguities associated with chemical composition, stoichiometry and stress in the future.

2 Materials and Methods

2.1 Samples

This study focuses on two gabbroic norite samples obtained from drill cores of the Mount Harcus Intrusion, which is a part of the Giles Complex, South Australia. The sample names 311.5 and 109.3 in Figure 1 correspond to their depth in m. The Giles-Event intrusions were emplaced into the Proterozoic Musgrave Province at about 1090-1040 Ma [*Maier et al.*, 2015]. The Harcus intrusion is of interest because of its striking *remanent* magnetic anomaly and the potential for magmatic nickel sulphide mineralizations [*Austin et al.*, 2014]. The high-coercivity remanent magnetization is interpreted to be carried by single-domain magnetite [*Church et al.*, 2016]. In reflected light the two thin sections in Figure 1 display a wide distribution of magnetite grain sizes, from large, discrete ($> 100\ \mu$m) multi-domain magnetite with oxy-exsolution of ilmenite lamellae and spinel needles and blades. Reduction exsolution of magnetite from ilmenite in the form of blades occurs in isolated ilmenite grains, and in some large ilmenite lamellae, which were first oxy-exsolved from magnetite [*Church et al.*, 2016; *Robinson et al.*, 2016]. Silicate-hosted micrometer- to nanometer-sized inclusions of magnetite are found in feldspars, pyroxenes and amphiboles ($\ll 0.1\ \mu$m). Primary silicates contain the highest concentrations of iron-oxide inclusions and were targeted for 3D imaging using FIB nanotomography. Both thin sections 311.5 and 109.3 are composed of plagioclase, pyroxene, amphibole, intragranular quartz and discrete iron-titanium oxides. Iron-oxide inclusions are present in primary plagioclase and pyroxene and secondary amphibole. Sample 311.5 has a high concentration of inclusions in plagioclase and amphibole. Metamorphic processes have possibly redistributed iron oxides in amphiboles. The intragranular quartz in association with amphibole also suggests the presence of fluids that may have mobilized Fe, and removed it from the system. Sample 109.3 has a lower amount of amphibole and iron-oxide inclusions in plagioclase balanced by an increase of iron-oxide inclusions in the pyroxene. For samples 311.5 and 109.3 the bulk natural remanent magnetization (NRM) values are 34 A/m and 4 A/m, and their bulk magnetic susceptibility values are 0.06 (SI) and 0.10 (SI), respectively.

2.2 Focussed-Ion-Beam Slice-and-View Nanotomography

Raw data collection was performed using the Auto Slice & View 4 software on an FEI Helios G4 UX Dual-Beam Focused-Ion-Beam (FIB) microscope at the NTNU NanoLab in Trondheim, Norway. Polished thin sections were coated with 10 nm of Au and the regions of interest wereanalysed with EDSto confirm that the target iron oxide inclusions were magnetite with minor (<1 wt%) Ti. At the optimal imaging settings for the selected minerals, the

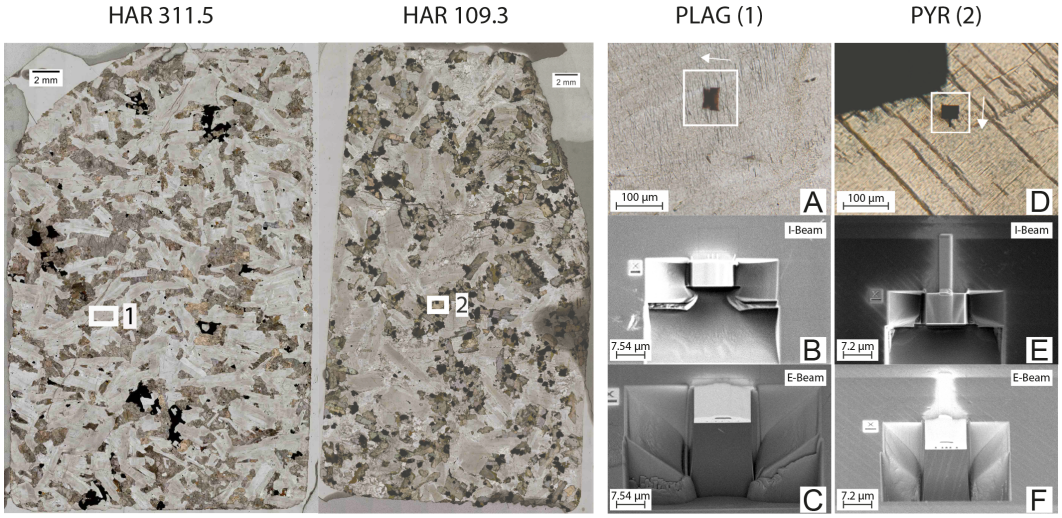

Figure 1. Thin sections 311.5 and 109.3 with slice-and-view locations 1 (plagioclase) and 2 (pyroxene). White arrows in (a) and (d) are aligned with the FIB slice-and-view milling direction (Z-axis). (b) and (e) Ion-beam view of the milling volumes outlined by the platinum protective layer. (c) and (f) Electron-beam view of the cross section (front face) of the milling volume. The electron beam is oriented at 52° to the ion beam.

electron beam drift was about 500 nm an hour, which limited the size of the block volume that could be successfully imaged. A block volume of material measuring 12x14x12 μm (L-W-H), sliced with 30 nm increments, took, on average, 20 hours. With longer sessions, the failure rate increased substantially. Block volumes were also limited by hardness of the material and the ability to successfully prepare the trenches and clean the front face of the sliced volume. The extracted volume of pyroxene is therefore smaller than for plagioclase since the ion-beam has fewer issues with removing material.

Sample preparation for slice-and-view was performed by manual instrument operation, outside of the automated software. The selected area was first coated with 500 nm of Pt. Five 200 nm deep lines that extend the full depth of the milling area were cut into the Pt coating and then filled by carbon deposition using the ion beam. The selected area was then covered with a further 300 nm of Pt. The central three carbon rods were orientated parallel to the slice direction and used as image alignment references. The outside two carbon rods were oriented at an angle of ±60° to the slice direction and were used to calibrate the slice thickness and to enable alignment of images in the slice direction in cases where there are missing images, or if a milling session had to be restarted. The surface preparation was finalized with 3 μm wide and 500 nm thick carbon rectangle, oriented parallel to the slice direction, and covered with an additional 300 nm of Pt. This carbon slab is used to keep the E-beam image aligned with the front face at all times. Trenches, 15 μm deep, 10-13 μm wide, and 10 μm long, were created to the left and right of the target volume, and a trench 20-25 μm wide and 20 μm long was created in front of the target volume using a standard cross section milling routine at 30 keV and 20 nA. The front and sides were then polished with cleaning cross sections, first at 1.2 nA and then with a final cleaning step at 0.75 nA. A Pt fiducial mark for ion beam alignment was placed on the thin section surface outside of the milled trenches as seen in I-beam and E-beam images in Figure 1.

For slicing, the Ga-ion beam was kept at 30 keV and 0.75 nA and slice thickness was chosen between 10 and 30 nm. Electron-beam imaging applies a mirror detector for the Backscattered-Electron (BSE) signal in immersion mode at 5 kV and 0.8 nA. Tilt correc-

tion for the 52° angle between the ion- and electron-beam was performed in the FEI software with dynamic focus by activating the tilt-correction option. Each scan with 6144x4096 pixels at 10 μs dwell time, resulted in a 1535x1652 image with pixel size of 7.5 nm in the pyroxene, a 2037x2043 image with pixel size of 7.6 nm in plagioclase. Early trials included the automatic z-axis drift equal to the milling depth and used a fiducial mark outside the milling area for consistent E-beam alignment. However, because this instrument has a constant E-beam drift that is not accounted by the software, it was found to be much more efficient to use the carbon slab as a fiducial mark that remains inside the milling area. This approach reduced the need for additional automated focusing steps after each slice. The high contrast between platinum and carbon, reduces the risk of losing the fiducial mark as the project runs, and increases the success rate of the automated procedure.

2.3 Image and object filtering

The raster images of the milled front faces are provided in Tagged Image File Format (TIF) and were stacked in Fiji (ImageJ) and aligned with the stack alignment plugin [*Tseng et al.*, 2011], using the cross-section of the three central carbon trenches as reference pattern. Using their high electron reflectivity and thus brightness, magnetite particles were extracted by gray scale thresholding and exported as binary images.Based on backscatter intensity and cross-referenced with the EDS analyses anything that we could not confirm as magnetite was segmented out. In the case of complex structures and overlapping threshold values, each slice was manually "cleaned" by going through the binary and image stack (side by side), removing any artifacts, or segmented threshold values that were not magnetite. For the pyroxene stack, the thresholding was particularly difficult because the bottom sections of each image had lower overall backscatter intensity than the upper parts. This image stack had to be treated with a non-local means filter, and was segmented using the Dragonfly software from ORS. After the binary segmentation, the stack was passed through 3x3x3 pixel 3D-mean and Gaussian-blur filters to smooth over the pixel boundaries, and to reduce sharp edges in objects at the boundary of the originally cropped volume. Areas with objects in close proximity to each other were manually edited to prevent bridging artifacts when converted to a finite element surface mesh. We excluded incomplete particles at the edge of the milled volume, and particles that are too small to be confidently distinguished from background and noise.

2.4 Mesh generation

The stack generated in Fiji was imported to Paraview [*Ahrens et al.*, 2005], then resized based on pixel length, width and slice thickness to regenerate the actual size of the milled volume. A surface mesh of the magnetic particles was generated using a contour filter based on the magnetite brightness threshold. The resulting initial mesh was exported as a stereolithography (STL) file. Both, Meshmixer [*Schmidt and Singh*, 2010] and Meshlab [*Cignoni et al.*, 2008] were then used to improve the meshes. The quality of each object was evaluated individually. An object was discarded if it did not intersect at least two slices. This imposes a lower-size limit of approximately 30 nm for particles to be modeled in 3D using this method. For geological time-scales, this corresponds approximately to the superparamagnetic transition size for magnetite. The geometric mesh quality for each object was checked, and any holes filled to generate a closed mesh surface. Surface mesh node-density was reduced to generate a more smoothed surface that minimizes the appearance of artificial steps reflecting the finite distance between the measured slices. After eliminating the voxel steps between the slices, mesh node-density was again increased to generate a now smoothed mesh with a target edge length $\leq$ 8.9 nm, the exchange length of magnetite. Target edge length, mesh quality and volume were checked in meshlab. If the mesh still contained artificial sharp edges due to the object's small size, it was remeshed and smoothed in Meshmixer to fit the original size. Iso2mesh and a Matlab script [*Fang and Boas*, 2009] were used to generated tetrahedral volume meshes from the surface meshes. Also here a target edge length $\leq$ 8.9 nm was used. To keep the node density similar for each object, the edge length was reduced for smaller ob-

jects. The output file was converted to a Patran file using Git Bash (Windows computer) to call a shell script (Convert2Pat) [*Ó Conbhuí et al.*, 2018]. The Patran file is then called by a script to be used by MERRILL for computing the magnetization structures. Aspect ratios of the final meshes were computed from the STL files based on the volume inertia tensor, by computing its eigenvalues and eigensystem by a Python routine. To ensure correct calculations, the proportional relationship between the eigenvalues was tested by comparing it to the measured short and long axis of the same particles in Meshlab.

2.5 Micromagnetic modelling

Micromagnetic modeling uses the Micromagnetic Earth Related Rapid Interpreted Language Laboratory (MERRILL), a micromagnetics package optimized for rock magnetism [*Ó Conbhuí et al.*, 2018; *Fabian and Shcherbakov*, 2018]. MERRILL applies finite element tetrahedral meshes to calculate local micromagnetic energies, and a boundary element method to calculate the demagnetizing energy and its gradient [*Ó Conbhuí et al.*, 2018]. For each particle in our study, first an initial remanent domain state was obtained by minimizing the total micromagnetic energy starting from a state of fully randomised spins. Next, for each particle the upper branches of 20 hysteresis loops between the maximal fields of 350 mT and -350 mT was calculated in 5 mT steps. Each of these hysteresis loops was calculated for one of 20 directions chosen from a Fibonacci sphere to achieve an approximately homogenous axis distribution. Backfield remanence curves from 0 to -200 mT in 5 mT steps were calculated for the same 20 field orientations starting from a positive saturation remanence state. While it is possible to run multiple MERRILL operations simultaneously, with the computer power available (Linux server with 20 cores and 128 GB memory) it was still necessary to limit the input file size because of the exponentially increasing time used for minimization. For file sizes < 20 MB an average hysteresis run took 15 min, and an average backfield curve required 35 min. It was possible to complete one hysteresis loop for 250 particles in two field directions within 24 hours. The total dataset presented in this paper equals to approximately 8000 hysteresis loops and 8000 backfield curves. The numerical average of the hysteresis loops and backfield curves over the 20 field directions for each mesh geometry approximately represents a random spherical ensemble of equal particles. Values of M_{rs}, H_c and H_{cr} were extracted from the average curves. Visual presentation of the magnetization structures of individual models was obtained using the open-source software ParaView (www.paraview.org) [*Ayachit*, 2015].

3 Results

3.1 Plagioclase

One cube measuring 12.77 μm × 14.50 μm × 12.77 μm (L×W×H) was extracted from plagioclase (PLAG (1) Figure 1 and Figure 2). This volume was reconstructed from 421 slices, each with a thickness of 30 nm. We extracted a total of 162 particles of magnetite and were able to run hysteresis loops for 140 of these. In this volume of plagioclase the magnetite forms two different patterns differentiated by shape and size. The first and most noticeable are magnetite "rods" that are a few to several micrometers long and often extend beyond the milled volume. In Figure 2 we observe these rods oriented in two sets of parallel directions. This observation suggests that these rods are crystallographically oriented, however, we would need to cross reference EBSD and magnetite long axis pole plots to confirm this. Cross sections show that these rods/needles either form flattened or prismatic shapes, with irregular gaps (red arrow in Figure 2) making most of these rods sequences of shorter pieces. The size and volume of these rods are too large to be run by MERRILL in a reasonable time (one smaller 6.6 μm × 0.2 μm magnetite rod was successfully minimized in zero-field from an initial state of randomised moments and shown in Appendix A.1). Figure A.1 show the general observation for magnetite rods that the magnetization aligns with the length of the rod and generates vortices at each end. The 140 smaller magnetite particles are a mix of

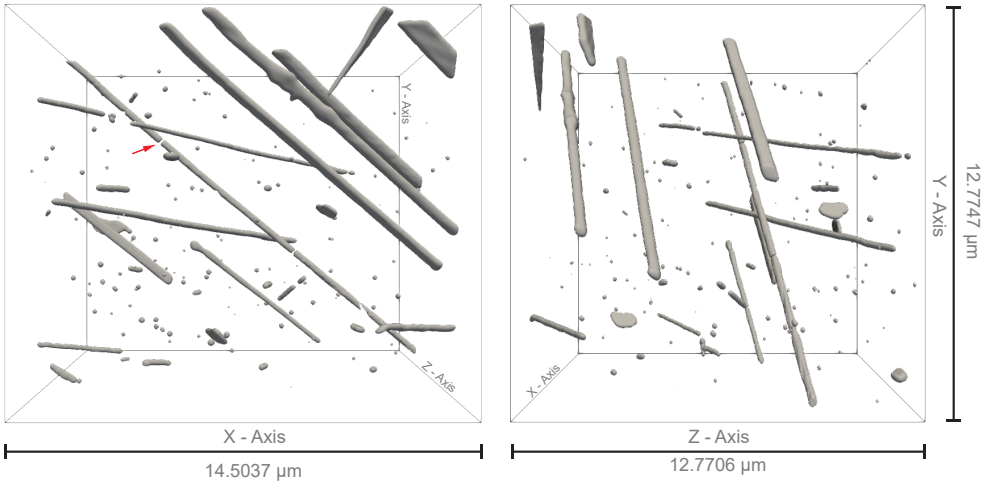

Figure 2. Magnetite inclusions in a 12.77 μm × 14.50 μm × 12.77 μm (L×W×H) volume of plagioclase, observed as rods and smaller rather oblate particles. Red arrow highlights the irregular gaps in the magnetite rods.

prolate, oblate and spherical particles with 0.71 median aspect ratio and 0.131 μm median equivalent sphere diameter (Figure 4). These are commonly associated with an unknown mineral with a lower backscatter intensity that was removed during electron reflectivity segmentation, as described in section 2.3 (Appendix A.2).

3.2 Pyroxene

The second volume is from pyroxene (PYR (2) in Figure 1) and measures 6.5 μm × 10.24 μm × 9.73 μm (L×W×H) (Figure 3). This volume is reconstructed from 647 slices with a slice thickness of 10 nm, which contained total of 282 magnetite particles of which hysteresis loops were calculated for 273. Magnetite in pyroxene forms elongated particles with a median 0.31 aspect ratio (Figure 4b) that are observed in three orientations. This silicate-oxide relationship is described by [*Fleet et al.*, 1980; *Frandsen et al.*, 2004; *Renne et al.*, 2002]. For the small magnetite particles included in this pyroxene dataset the Ti content is expected to be low. The largest object does show sections that contain higher Ti values and is excluded from this dataset. EDS overview maps for areas with small particles also contain trace amount (< 1 wt%) Ti, but there is no visible change in the backscatter intensity, nor any Ti peak in EDS spot analysis and we can therefor not confirm where the Ti is located. Due to the size of the smaller objects and the spot size of the SEM there is a possibility that the magnetite contain sections that are higher in Ti (ulvöspinel or ilmenite). TEM or Microprobe is needed to quantify the Ti content and confirm the mineral identification. Based on the cited papers above there is good confidence to identify these smaller inclusions as magnetite.

Figure 4 and Appendix A.5 summarizes sizes (A) and aspect ratios (B) for the modelled particles in both plagioclase and pyroxene. The "equivalent sphere diameter" is calculated from a sphere with equivalent particle volume. The aspect ratio was calculated using the ratio of min over max eigenvalues of the moment of inertia. The complete dataset presented in Figure 4 is subdivided according to both the type of silicate host and the zero-field-minimized magnetic state (Figure 5 and Table 2). For SD particles we observe a median size difference between particles hosted by plagioclase (0.062 μm) versus pyroxene (0.107 μm). The plagioclase-hosted magnetite particles have a difference in shape, with median aspect ratios of 0.63 compared to 0.26 for pyroxene-hosted magnetite. The difference in shape is

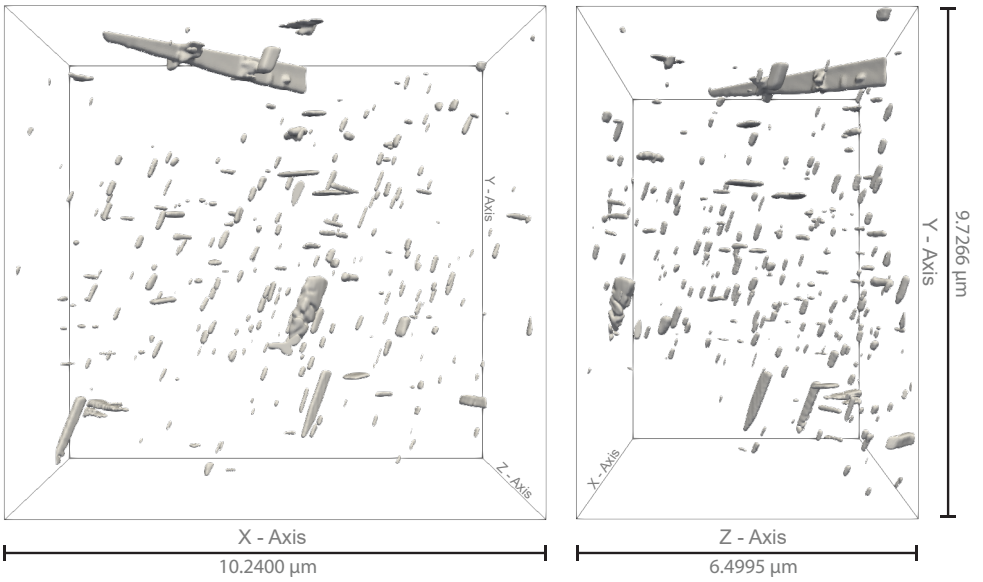

Figure 3. Magnetite inclusions in a 6.5 μm × 10.24 μm × 9.73 μm (L×W×H) volume of pyroxene, observed as mainly prolate shapes in three orientations.

also observed for SV particles, with median size and aspect ratio of 0.144 μm and 0.72, respectively, for plagioclase and 0.159 μm and 0.4, respectively, for pyroxene. The shape difference is not observed for MV particles, however, with median size and aspect ratio of 0.247 μm and 0.24, respectively, for plagioclase and 0.214 μm and 0.26, respectively, for pyroxene. There are three particles characterized as having SW ("swirl") domain structure (Appendix A.3). This group refers to a distinct set of large grains with low aspect ratios (median size of 0.370 μm, and aspect ratio of 0.2 that represents a particle 0.500 μm long and 0.100 μm wide). These particles were observed only within pyroxene and, because of their large size we were only able to complete 20 hysteresis runs for these three particles. We were unable to complete backfield runs due to insufficient computer memory.

3.3 Domain characterization

Figure 5 shows the micromagnetic states of representative particles and how they were categorized after minimizing their total magnetic energy from random initial moments. The domain state estimations represent one of many possible local energy minima. The minimization from random initial moments should ideally be repeated multiple times to categorize the full range domain states, and potentially identify the global energy minimum state. This is computationally expensive, but should be encouraged for future studies and as a part of the FIB-nt method in general. Insets show the corresponding average hysteresis loop for each particle. The arrows are color coded by their vertical (M_z) component where up = red and blue = down. The vortex core is represented by contour surfaces (in green) enclosing volumes with increased helicity of the magnetization field **m** defined by

$$\mathrm{hel}\,\mathbf{m} \;=\; \mathbf{m}\cdot(\nabla\times\mathbf{m})\,.$$

Single domain (SD) particles have uniform magnetic moments aligned throughout the particle, although the spins may bend along the demagnetizing field lines at edges and corners (flower state). The single vortex (SV) is a inhomogenous magnetization state with lowest total micromagnetic energy beyond the single domain limit [*Hubert and Schäfer*, 1998].

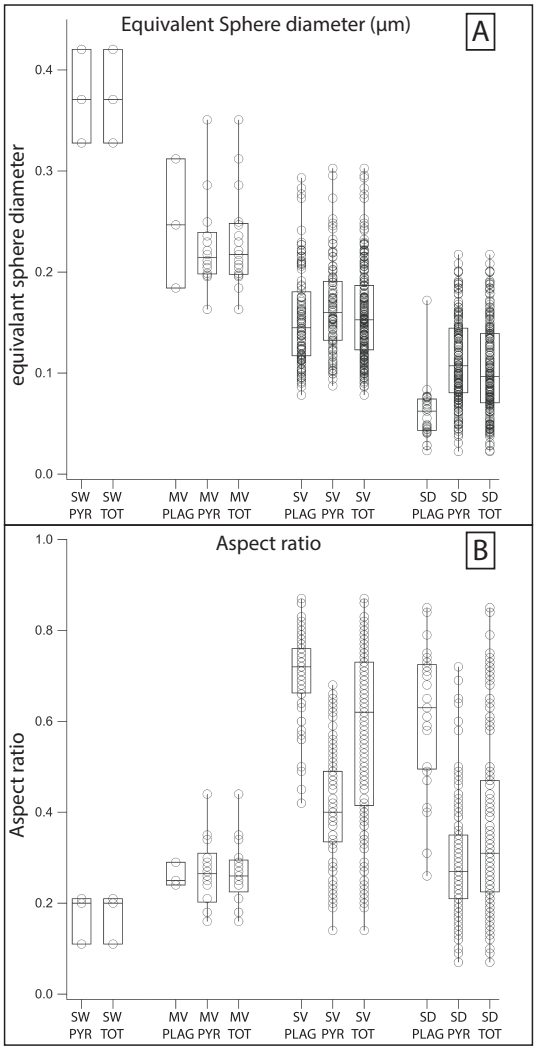

348 **Figure 4.** Box plots that show the relation of particle size (A) and aspect ratio (B), subdivided according to
349 the host silicate (plagioclase and pyroxene) and the modelled micromagnetic domain structure (single domain,
350 single vortex, multi vortex, swirl).

366 The net energy decrease is obtained by reducing the magnetic stray-field energy through flux
367 closure at the expense of increasing exchange and anisotropy energy. Therefore this transi-
368 tion can only occur when the decrease in demagnetizing energy overcompensates this in-
369 crease. Visually, the single vortex core extends partially or fully through the particle. *Rave*
370 *et al.* [1998a]; *Hubert and Schäfer* [1998] find that there is a transition from a simple vortex-
371 state to a well-defined multi-domain state, where vortices are embedded features within the
372 soft-magnetic Bloch walls. In this paper this transition is described as a multi vortex (MV)
373 state from the zero-field minimization. The MV state is characterized by the presence of two
374 or more well-defined vortex cores that create a continuously varying directional change in
375 magnetization, as opposed to an abrupt angular change that would indicate a domain wall.
376 Similar observations have been made in much larger (1.4 μm) pyramidal titanomagnetite
377 particles [*Khakhalova et al.*, 2018]. Particles with fully developed 90 ° domain wallswere
378 in general too large for our server to minimize hysteresis and backfield curves in 20 field
379 directions in MERRILL. *Nagy et al.* [2019] did model cuboctahedral magnetite from 0.03-
380 2.7 μm equivalent sphere volume diameter and 0.03-1.5 μm magnetite spheres, studying the

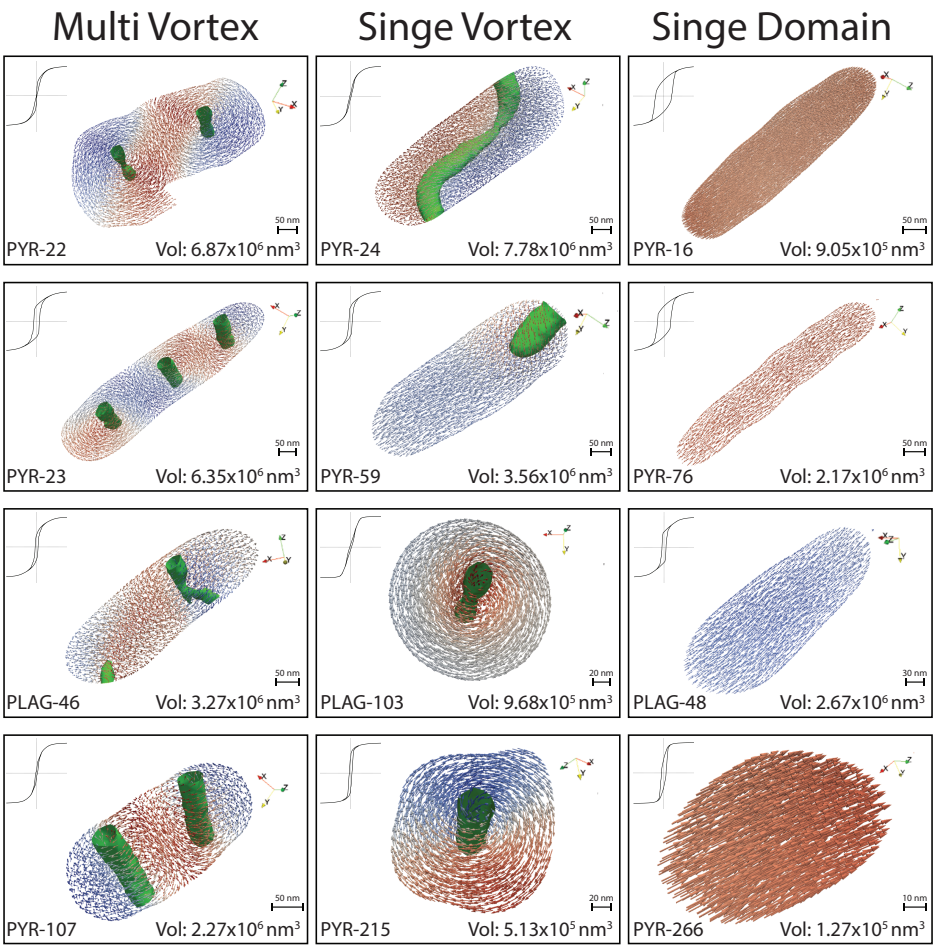

Figure 5. Magnetic models that express the variability of magnetic signatures within each classification. Insets show the simulated average hysteresis loop for each particle, with normalized moments and external field from +350 to -350 mT. Arrow colors show the M_z component, red = up and blue = down. Green contour (vortex core) represents areas of increased helicity of the magnetization field. Hysteresis, size and shape parameters for each individual particle are summarized in Table 1. Location of these twelve particles are marked with bold text in the subsequent figures 7, 8, 9, 10 and 11.

evolution of domain structures in magnetite grains with different sizes. They observed the formation of primitive bloch-like 71° domain walls that separate uniform regions of magnetization, similar to our observations in the three selected large particles in Appendix A.3. In these particles the magnetization pattern mainly consists of vortices or swirls that represent seeds of Bloch walls, but due to size constraints, cannot develop into conventional domain walls as they occur in well-developed multi-domain patterns [*Fabian et al.*, 1996; *Hubert and Schäfer*, 1998]. Domain walls widths expected for MD magnetite are observed only in much larger particles (~ 3 μm) and the SV structures are present until at least ~ 1 μm [*Nagy et al.*, 2019]. Due to the lack of a distinctive terminology, the intermediate sized magnetite structures are defined as "swirl" (SW) within this paper.

Table 1. Hysteresis(f=femto), diameter (equivalent sphere diameter) and aspect ratio parameters of the average hysteresis loops for the individual particles inset in Figure 5 and highlighted with bold text in Figure 7, 8, 9, 10 and 11.

Particle	M_s (fAm^2)	M_{rs} (fAm^2)	H_c (mT)	H_{cr} (mT)	Diameter (μm)	Aspect ratio
PYR-16	0.43	0.223	92.7	115.3	0.120	0.19
PYR-22	3.30	0.281	3.35	20.6	0.236	0.21
PYR-23	3.05	0.157	32.4	41.8	0.230	0.16
PYR-24	3.74	0.326	8.8	44.4	0.246	0.34
PYR-59	1.71	0.789	18.9	32.7	0.189	0.28
PYR-76	1.04	0.519	76.7	94.3	0.161	0.13
PYR-107	1.09	0.114	9.53	26.6	0.163	0.44
PYR-215	0.246	0.120	15.3	29.0	0.099	0.47
PYR-266	0.061	0.028	26.7	42.8	0.062	0.69
PLAG-46	1.57	0.628	16.9	29.8	0.184	0.29
PLAG-48	1.28	0.644	23.7	34.6	0.172	0.31
PLAG-103	0.465	0.404	9.8	48.2	0.123	0.73

Table 2. Particles categorization of domain state that are hosted by their respective silicate.

Silicate	SD (green)	SV (red)	MV (blue)	SW (purple)	total
Plagioclase	29	108	3	0	140
Pyroxene	159	97	14	3	273

3.4 Hysteresis loops

Hysteresis results for all simulated inclusions, from both plagioclase (circles) and pyroxenes (triangles), are summarised in Figure 6, Figure 7 (Day plot), Figure 9 (Néel plot), Figure 11 (Butler-Banerjee plot) and Appendix A.5. Each point represents the average hysteresis data acquired from 20 different field directions and is colour coded according to the remanent domain state observed at zero field following energy minimisation from a random starting configuration (purple = SD, yellow = SV and turquoise = MV). Each symbol size is scaled according to particle size, defined as the diameter of a sphere with equivalent volume. The total number of particles adopting each remanent state is represented in Table 2.

The two red markers (one for each silicate) in Figures 7 and 9 represent the average hysteresis properties for all of the modelled particles. Assuming the two volumes studied provide a representative sample of the silicate-hosted component of magnetic mineralogy, these two points provide an estimate of the hysteresis properties that would be obtained if we measured the bulk properties of plagioclase and pyroxene extracts experimentally. These 'bulk' hysteresis properties would normally be the only two points available to perform domain state diagnosis. However, when deconstructed to individual particles, we observe the data for both volumes extends across the entire range of the common diagnostic diagrams and all regions designated to specific domain states. The location of these bulk average points also suggest the domain states are unevenly distributed between the silicates. The bulk average for pyroxene is dominated by SD particles and for plagioclase is dominated by SV particles (Table 2). Figure 6 shows the distribution of particles between the domain states, host silicate and M_{rs}/M_s ranges. For SD there is a distinct separation, with tight clusters of M_{rs}/M_s ranges with pyroxene hosted particles at 0.5 and plagioclase hosted particles at 0.7. For SV particles there are M_{rs}/M_s values where particles form clusters. Within plagioclase SV particles cluster at M_{rs}/M_s values $\approx 6.1\times10^{-2}$, but there are a few points that extend the range up to $M_{rs}/M_s = 0.7$. SV particles in pyroxene show a bimodal distribution (red boxes)

with clusters at M_{rs}/M_s values > 0.3 and < 0.3. MV particles show a similar tendency to form two separate clusters at M_{rs}/M_s values ≈ 0.1 and 0.4. This is most evident for particles hosted by pyroxene, but with only three particlesextracted from the plagioclase is an insufficient sample size to indicate anything about specific M_{rs}/M_s ranges. What we have for now indicates that these particles cover the same M_{rs}/M_s ranges as MV magnetite in pyroxene. Three SW particles hosted by pyroxene did successfully complete minimizationof the hysteresis loop. The spread in M_{rs}/M_s is from 0.12 to 3.44×10^{-4}.

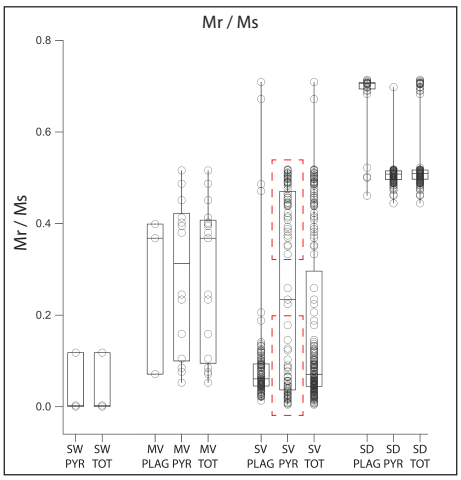

Figure 6. Box plots for the statistics of individual magnetite M_{rs}/M_s in plagioclase, pyroxene and combined total for the different modelled domain structures.

3.5 Day plot

In Figure 7 the SD particles plot in the expected region at $M_{rs}/M_s \approx 0.5$. SV particles span the whole range from SD to MD. MV particles tend to plot towards the upper left with M_{rs}/M_s values > 6.0×10^{-2} and $H_{cr}/H_c < 7$. The spread of points shows little regard for the particle size, highlighted by Figure 8, where particles with varying sizes and domain states coexist and even overlap. This observation is also evident throughout Figure 7. At M_{rs}/M_s values ≈ 0.5 the cluster of prolate particles is mainly hosted by pyroxene. SD particles hosted by plagioclase form a cluster at M_{rs}/M_s values ≈ 0.7.

3.6 Néel plot

In a Néel plot (Figure 9) we observe a dominating SD "central ridge" that extends from 10 mT < H_c < 120 mT. The SD particles mainly hosted by pyroxene at $M_{rs}/M_s \approx 0.5$ align with the uniaxial SD (USD) theoretical line. Axis ratios show the majority of these particles are prolate in shape (Appendix A.4), and correspond to the median aspect ratio cluster of 0.26 (Figure 4b). The feldspar-hosted SD particles (higher median aspect ratio of 0.62 in Figure 4b) form a cluster at M_{rs}/M_s values ≈ 0.7 and 10 mT < H_c < 30 mT. These particles are oblate spheroids and the increase in H_c for these particles represents a general increase in particle oblateness/flatness (Figure 9A). The low-coercivity (< 10mT) region is dominated by SV and MV particles. With decreasing coercivities below 10 mT, there is also a decrease in M_{rs}/M_s. Particles with M_{rs}/M_s values < 0.3 form a distinct cluster that is dominated by SV states (Figure 10). This cluster has a well-defined trend for particles from both plagioclase and pyroxene. While pyroxene-hosted particles are equally sized and evenly distributed in Figure 10, there is a decrease in particle size in plagioclase above $H_c \approx 9$ mT. Particles below 9 mT and $M_{rs}/M_s = 0.07$ align with the theoretical "USD + SP". Those above 9 mT

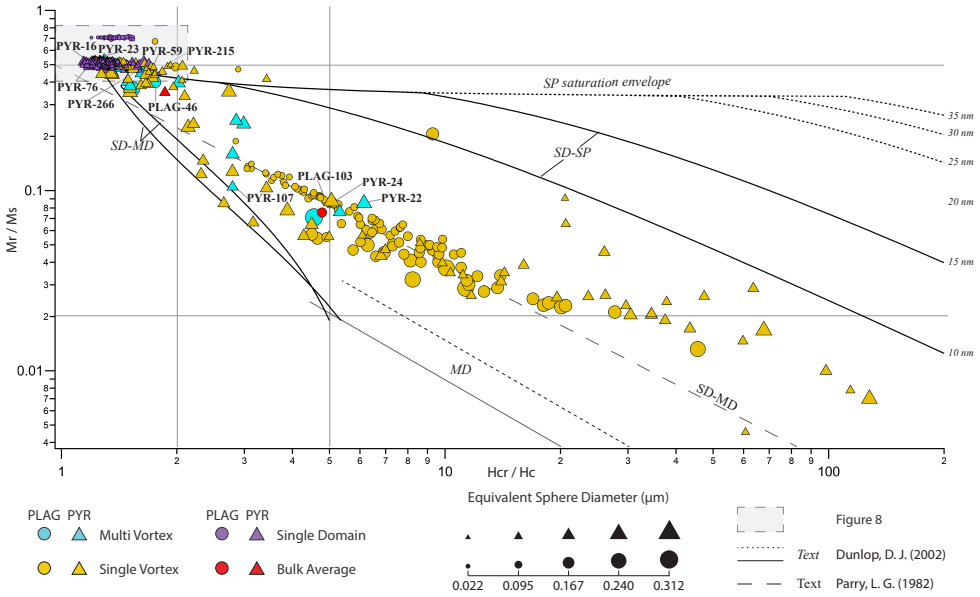

435 **Figure 7.** Day plot with theoretical mixing curves of *Dunlop* [2002] and *Parry* [1982]. Regions for SD,
436 PSD and MD from *Dunlop* [2002]. Bold text indicates the positions of particles from Figure 5 and Table 1.

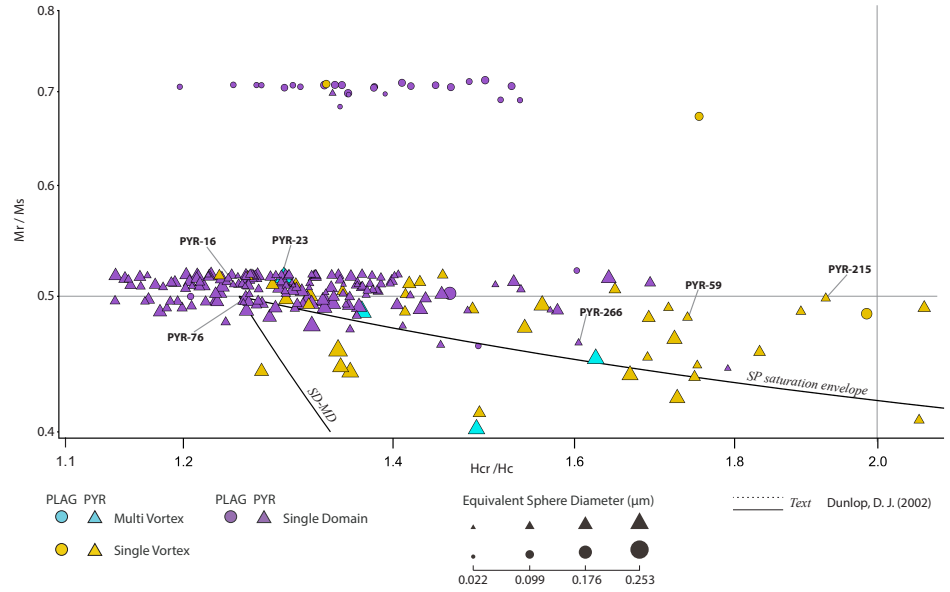

437 **Figure 8.** Expanded area of Figure 7 showing the SD clusters at $M_{rs}/M_s > 0.43$ and $H_{cr}/H_c < 2.4$. Bold
438 text indicates the positions of particles from Figure 5 Table 1.

demonstrate an increased upwards slope that follows the USD theoretical lines from *Tauxe et al.* [2002].

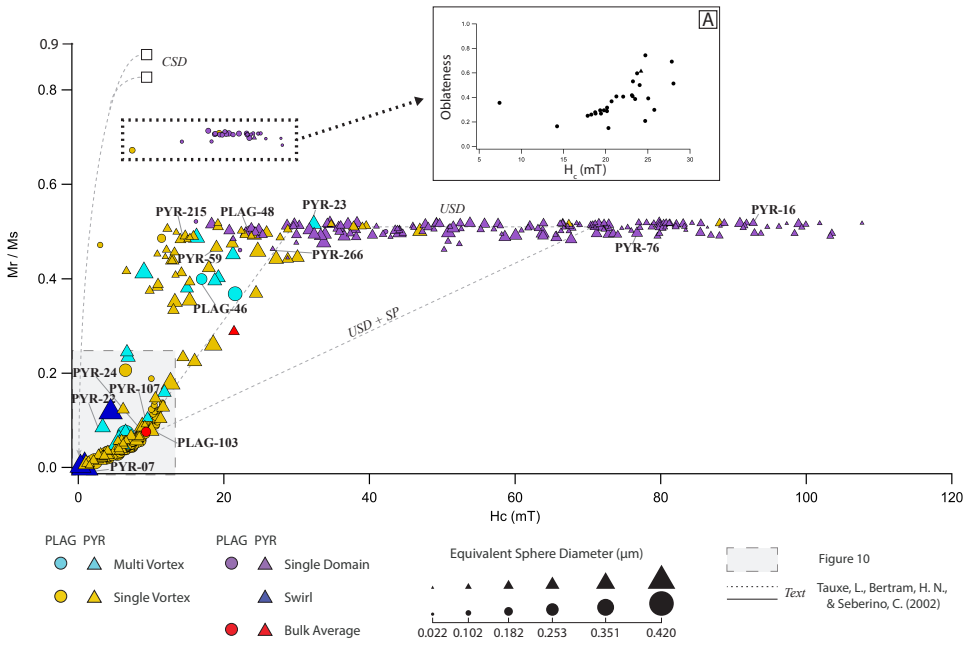

Figure 9. Néel plot with the location of particles from Figure 5 in bold and Table 1. Theoretical lines of USD, USD+SP and CSD from *Tauxe et al.* [2002]. Inset (A) shows the increasing oblateness for the SD particles at $M_{rs}/M_s = 0.7$ with increasing H_c.

3.7 Butler-Banerjee plot

The Butler-Banerjee plot in Figure 11 delineates a two-dimensional size-shape range for SD particles of magnetite and titanomagnetite [*Butler and Banerjee*, 1975]. Contrary to the Day and Néel plots, which interpret domain state from hysteresis parameters, the Butler-Banerjee plot predicts domain states based on the length of a particle's long axis compared to its axis ratio. One is therefore able to characterize a particle's domain state purely based on shape and size. The theoretical boundaries in the background were calculated either by a domain model [*Butler and Banerjee*, 1975] (dashed line) or by 3D micromagnetic modeling [*Muxworthy and Williams*, 2008] (solid lines). In *Butler and Banerjee* [1975] the particles have cuboidal shapes with 180° domain walls, while in *Muxworthy and Williams* [2008] the magnetic particles are SD or SV parallelepipeds arranged in chains to assess magnetostatic stabilization in chains of magnetosomes from magnetotactic bacteria. Our dataset defines a clear transition between SD and SV states that is in good agreement with the 'no interaction' boundary identified by *Muxworthy and Williams* [2008] for isolated parallelepipeds. Our data in Figure 11 clearly reflect the influence of the silicate host mineral on the inclusion shape and subsequently its magnetic properties. While plagioclase-hosted magnetites (circles) plot predominantly at aspect ratios (AR) above 0.6, pyroxene-hosted magnetites (triangles) have AR less than 0.6. Particles that are able to adopt MV remanence states typically plot in the region with AR < 0.4 and long axis > 0.300 μm. The phase boundary between SD and SV/MV states in this region deviates from that of *Muxworthy and Williams* [2008], most likely reflecting the difference between the real particle geometries used here versus the ideal parallelepipeds used by *Muxworthy and Williams* [2008]. Figure 11 demonstrates that

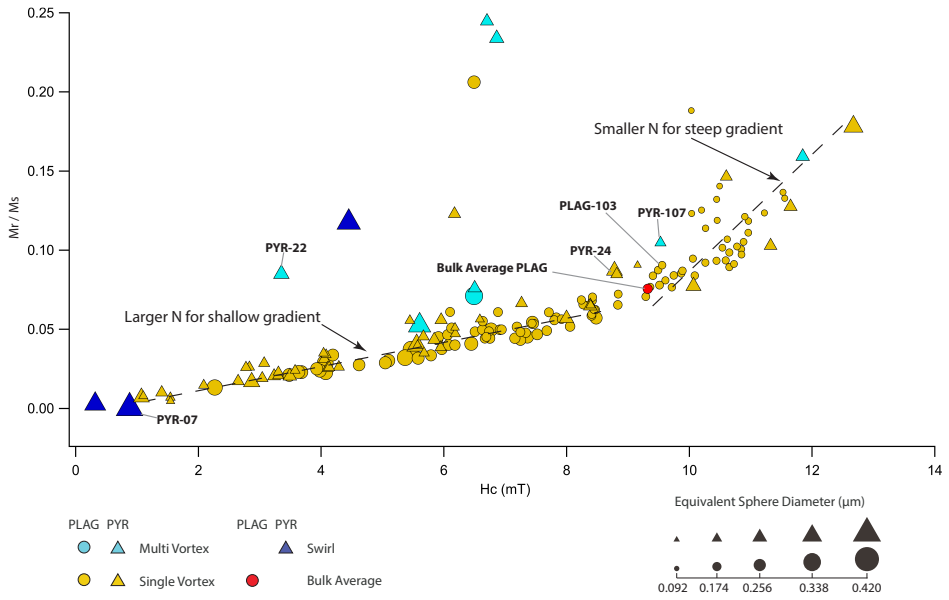

Figure 10. Expanded area of M_{rs}/M_s < 0.25 and H_c < 14mT from Figure 9. Bold text indicates particles from Figure 5, Table 1 and the bulk average for plagioclase. Particle PYR-07 is displayed in Appendix A.3.

MV and SW particles start to dominate over SV states with decreasing AR and increasing long axis length.

4 Discussion

As micromagnetics takes us beyond the SD theories that have been the foundation of rock magnetism since the pioneering work of Néel, the ability to obtain an accurate breakdown of the different classes of magnetic behaviour that exist within a sample becomes increasingly important. One of the most striking results of this study is the shear range of magnetic domain states and hysteresis properties that are observed within just two small $\sim 10\mu m^3$ volumes of silicate. The observed behaviour spans the entire range of popular domain-state diagnostic plots (Figures 7, 9 and 11). In contrast, bulk hysteresis measurements reduce this complexity to a single average data point (e.g. the red points in Figures 7, 9), discarding valuable information about the true nature of the underlying magnetic ensemble. Classifying a bulk sample as either 'SD', 'PSD', or 'MD' on the basis of the Day diagram is clearly meaningless when particles in the SV state plot across the entire 'SD/PSD/MD' range, and the largest MV particles plot much closer to the SD region than the MD region (Figure 7). Of the three diagnostic plots explored here, the most successful is the Butler-Banerjee plot (Figure 11). This diagram works well because it recognises the fundamental importance of particle size and shape as the dominant factors controlling the domain state of magnetite. However, our results also demonstrate that size and shape alone are often poor predictors of magnetic hysteresis properties. Generalised geometric information, such as equivalent spherical volume, is not sufficient to predict the magnetic properties – the specifics of individual particle geometries really do matter. Although time consuming and computationally intensive, the FIB-nt-FEM workflow presented here provides a route to rock magnetic characterisation that not only yields a quantitative breakdown of the domain states present, but a realistic estimate of the range of magnetic properties associated with the particle ensemble. As the database of magnetic properties linked to specific particle geometries expands, it will eventually become possible to use look-up tables and/or machine-learning approaches to translate 3D particle geometries into useful magnetic parameters (including, for example,

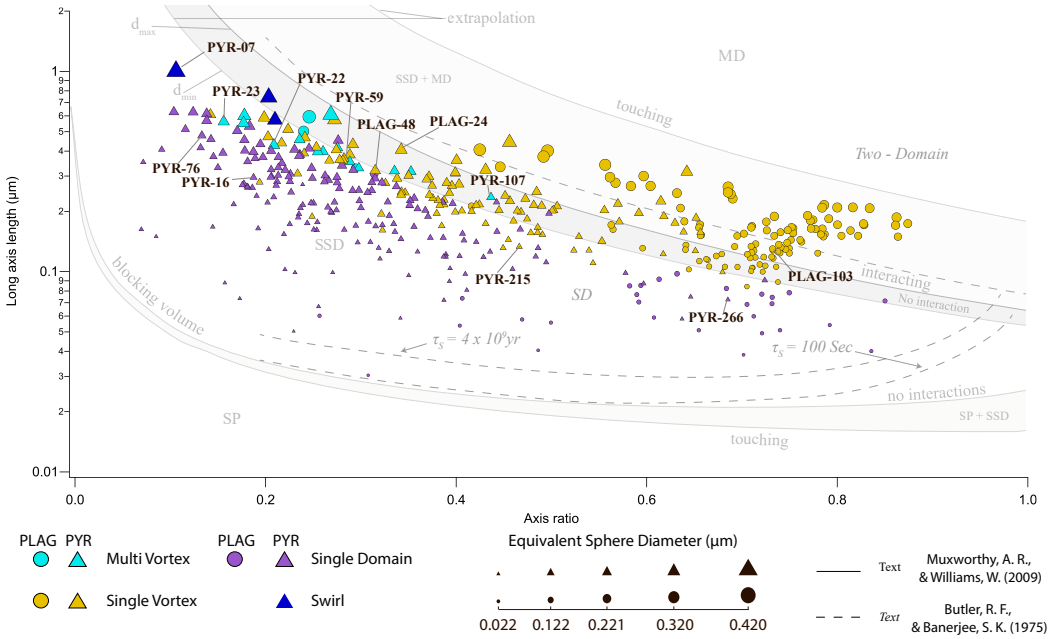

Figure 11. Butler-Banerjee diagram that shows the relationship between a particle's long axis and its axis ratio. Axis ratio = 0 references an infinitely long needle and axis ratio = 1 references an equidimensional particl (e.g. cube or sphere). Bold text indicates the position of particles visible in Figure 5 and Table 1, except for particle PYR-07 which is displayed in Appendix A.3.

energy barriers for thermal switching) without the need to perform additional micromagnetic simulations. With increased automation, the experimental methods outlined here could indeed become a routine feature of future rock magnetic characterisation workflows.

The Néel plot (Figure 9) shows a distinct "central ridge" of SD particles along the USD line at $M_{rs}/M_s \approx 0.5$. *Tauxe et al.* [2002] argue that the H_c increase for SD particles is proportional to an increase in the length to width (L/W) ratio. Figure 4a in *Tauxe et al.* [2002] shows that the increase from H_c = 30 mT to 70 mT for USD particles is caused by an increase in L/W from 1.3:1 to 2:1 While we do observe that particles with H_c >100 mT have high L/W ratio ($> 10:1$), for coercivities < 100 mT we do not find a clear correlation between coercivity and aspect ratio, which may be due to the large spread of USD particle sizes (0.022-0.253 μm). Our data imply that the size of a USD particle is at least as important as its aspect ratio in determining the switching field, highlighting again the need for detailed geometrical information to produce an accurate prediction of the magnetic properties of an ensemble. Another interesting modeling result is that the characteristic coercivity range for SD magnetite particles predominantly covers the range 10 mT< H_c <100 mT, which is in line with experimental results [*Church et al.*, 2016]. Without external stress, higher H_c values appear to require very unusual particle geometry, while SD structures with $H_c < 10$ mT can occur only in a very narrow grain size and shape region.

A cluster of feldspar-hosted SD particles with M_{rs}/M_s values of 0.7 (Figure 9 and 8) falls in between the theoretical values for cubic SD (M_{rs}/M_s = 0.83-0.87) [*Joffe and Heuberger*, 1974; *Tauxe et al.*, 2002] and uniaxial SD (M_{rs}/M_s = 0.5). This remanence ratio is similar to the value of M_{rs}/M_s = 0.75 calculated by *Harrison et al.* [2019] for particles with a combination of uniaxial anisotropy (restricting moments to a basal plane) and hexagonal anisotropy (defining multiple easy axes within that basal plane). This cluster contains mainly oblate particles (Appendix A.4), and therefore the intermediate value of M_{rs}/M_s is entirely consistent

Table 3. Individual particles with different magnetization structure that are all within the designated SD area of the Day plot

Object		M_{rs}/M_s	H_c (mT)	H_{cr} (mT)	Aspect Ratio	Sphere Diameter (μm)
PYR-137	SD	0.516	34.2178	46.4489	0.31	0.142
PLAG-146	SD	0.500	42.2442	50.9584	0.41	0.062
PYR-197	SV	0.519	19.1958	27.875	0.49	0.111
PLAG-135	SV	0.709	19.3504	25.7931	0.71	0.078
PYR-23	MV	0.516	32.3692	41.8226	0.16	0.229
PYR-21	MV	0.490	16.2453	22.2288	0.18	0.249

with these particles having a mixed uniaxial/multi-axial anisotropy. A positive correlation between coercivity and oblateness is observed (inset to Figure 9). This improved correlation may be a result of the smaller size variations within this oblate cluster (0.023-0.090 μm) compared to that of the pyroxene-hosted USD prolate cluster.

The SV domain state is observed across a wide range of particle sizes and shapes, and produces correspondingly large ranges of H_c (0-88 mT), M_{rs}/M_s (0-0.7) (Figure 9) and H_{cr}/H_c (1.5-107) (Figure 7). The SV particles in Figure 6 belong to different shape clusters, where PLAG contains more oblate and PYR more prolate particles with respect to the shape classification in Appendix A.4. For a constant demagnetizing factor (N), one would expect a linear increase of M_{rs}/M_s with H_c with slope inversely proportional to N (Figure 4.5 in *Stacey and Banerjee* [1974] and Figure 5.16 in *Dunlop and Özdemir* [1997]). The increased slope of the M_{rs}/M_s vs H_c plot for $H_c > 9$ mT (Figure 10) indicates, therefore, a smaller average demagnetizing factor for the smaller particlescompared to the larger particles with $H_c < 9$ mT (Appendix A.6).

Another key result of this study is the observation of SV and MV particles that display hysteresis properties similar to those expected for much smaller SD particles (Table 3). The MV state is stable in large grains (median 0.225 μm) with low aspect ratios < 0.5 (Figure 4a and b). Despite their larger sizes, these particles plot more towards the upper left of a Day diagram (SD and PSD regions), rather than towards the MD region. Large, slightly flattened needle ($a >> b > c$) particles with low aspect ratio readily adopt MV states during zero-field relaxation from a random starting configuration (e.g. PYR-23 in Figure 5), but are forced into a uniformly magnetised remanence state after exposure to a saturating field. This produces an apparent disconnect between the domain-state classification used in this study and the observed hysteresis properties. This disconnect becomes significant if, as intended, the zero-field relaxation state is more representative of a weak-field thermoremanent magnetisation (TRM) state than the corresponding saturation remanence state. Such disconnects have been observed in dusty olivine by *Lappe et al.* [2013], where stable SV states were observed after acquisition of weak-field TRM but were converted to metastable SD states after application of a room-temperature saturating field. Our study raises the question of whether high-field hysteresis measurements are always a useful means to classify the potential weak-field remanence states adopted by a given particle geometry, especially for SV and MV states, which may well be the dominant carriers of remanent moment. Such ambiguities are avoided using the FIB-nt-FEM approach, ensuring that an appropriate combination of physical models is always used for a given ensemble. A full theory of the remanence state adopted by such particles requires us to calculate the multitude of energy barriers between all possible remanent states. Although this is an active area of research, it is outside the scope of the current study. As discussed above, the state adopted will be highly dependent on the external field history. By introducing the energy barrier calculations, we would expect to see a better separation line between the remanence states of all the particles, resulting in adjustments to the theoretical lines in Figure 11 from *Butler and Banerjee* [1975]; *Muxworthy and Williams* [2008].

583 The blue particles seen in Figure 9, 10 and 11 are large (0.370 μm median equivalent
584 sphere diameter) oblate to prolate shapes (Figure 4a, b and Appendix A.4) which show a ten-
585 dency to form domain walls when minimized in zero-field (Appendix A.3). The backfield
586 curves were not able to be calculated on a reasonable timescale, and therefor are not plotted
587 on a Day diagram (Figure 7). On a Néel diagram (Figure 9), two SW particles plot close to
588 the origin, as would be expected for MD behaviour. One, however, displays similar proper-
589 ties to MV particles, suggesting that they share many characteristics, and that the transition
590 from MV to SW to MD is likely gradual onefor particles with this shape.

591 In Figure 7 the theoretical Day plot SD-MD and SD-SP mixing lines show the mod-
592 ified calculated binary curves *Dunlop* [2002] and the SD-MD mixing curve derived from
593 natural magnetite mixtures in *Parry* [1982]. Because effects like thermal variations, stress,
594 interactions, impurities or inclusions are not included in the models of this study, the hystere-
595 sis properties of our modelled particles represent ideal magnetite crystals. When the entire
596 data set is compared to theoretical mixing lines, the closest agreement occurs for the SD-MD
597 mixing line from *Parry* [1982], that represents a grain-size trend of measured mixtures of
598 SD and MD particles. The samples used by *Parry* [1982] were generated by crushing natu-
599 ral MD magnetite and sieving for various grain sizes. Because crushing introduces internal
600 stress anisotropy that may be larger than the magnetocrystalline anisotropy, the correlation
601 with our dataset appears to be spurious, but based on the fact that our data consistently lie
602 above the binary mixing lines from *Day et al.* [1977]; *Dunlop* [2002].

603 It is unavoidable that the magnetic models presented here contain several uncertainties
604 related to reconstruction artifacts, model assumptions, and unknown physical influence fac-
605 tors. Shape uncertainty is directly connected to the extraction of selected mineralogy from
606 the binary stack and the accuracy of the resulting finite-element meshes. The alignment of
607 fiducial marks in the image stack to reconstruct the volume contributes to the shape uncer-
608 tainty. The carbon rods are deposited from carbon gas reacting with the ion beam. As ob-
609 served in the reassembled stack, there are irregular shifts in image placement that also im-
610 pact the reconstructed shape, especially of the smallest particles. Evidence for this is seen in
611 the meshes as irregular pinching in elongated particles, where images are shifted. Thresh-
612 olding in FIJI is another uncertainty in reconstructing the true shape of particles. With the
613 variation in size, the extraction of the smaller particles will become suppressed when se-
614 lecting the threshold based on the median size. A simple calculation of the volume change
615 when increasing the particle volume by adding a pixel in each direction leads to an estimate
616 of up to 10-25% for the larger particles and 50-130% for the smaller particles (based on an
617 increase in the representing sphere diameter of 7 nm pixel width). The true change in vol-
618 ume is dependent on more complicated measures such as the particle orientation and the
619 milling thickness. We were also concerned that variable amount of mesh smoothing would
620 possibly change the hysteresis parameters and therefore the domain state. To test this we cal-
621 culated average hysteresis properties for 3 particles of different sizes at 3 different stages of
622 smoothness. First stage is where the particle shape is strongly voxelated (directly from the bi-
623 nary image), second is at intermediate smoothing and the last where all sides are completely
624 rounded (axis ratio is preserved in all stages). From the resulting hysteresis properties we
625 did not observe any significant changes beyond the deviation expected for models starting
626 with randomized moments. This is in agreement with a study by *Rave et al.* [1998b] that at
627 resolutions below the exchange length, particle surface discretization does not influence mi-
628 cromagnetic model results. Model assumptions that contribute to the overall uncertainty are
629 the material parameters for magnetite that in the natural minerals can vary for example due
630 to impurities. Physical unknowns are lattice orientations, related to the direction of the easy
631 anisotropy axes, or internal stress [*Hodych*, 1990; *ter Maat et al.*, 2020].

632 This study presents a workflow for extracting the 3D geometry of a nanoscale mag-
633 netic particle ensemble and calculating its micromagnetic properties. To date it is the most
634 comprehensive micromagnetic data set of natural remanence carriers, and acts as a proof-of-
635 concept study for obtaining statistical data on the magnetic domain state and hysteresis prop-

erties of silicate-hosted magnetic inclusions. This work is of particular relevence to single-crystal paleomagnetic studies, which offer the best possibility of extracting reliable primary paleomagnetic remanence data from ancient rocks with complex geological histories. The key challenge in such studies is targeting primary remanence carriers that are most likely to have escaped thermal, chemical or viscous remagnetization. In the case of the Harcus intrusion, stable remanence carriers hosted in primary feldspar and pyroxene grains could be targeted directly, avoiding both remanence carriers hosted by secondary amphibole as well as interstitial MD magnetite that could carry a viscous overprint. The combination of FIB-nt and micromagnetic simulations provides a full statistical breakdown of the domain states present in a representative single crystal. Further studies will enable the range of local energy minimum states adopted by the SD, SV, MV, SW and MD states, as well as the energy barriers that separate them, to be calculated, and the corresponding blocking/unblocking behaviour during natural and laboratory cooling/heating cycles to be modelled. With that we would be one step closer to a comprehensive model of remanence acquisition that takes us beyond Néel's SD theory. Ultimately this will increase both the reliability of single-crystal paleomagnetic studies and our confidence to interpret them, paving the way to unlocking hitherto inaccessible parts of the geomagnetic record.

5 Conclusions

1. FIB-nt protocols have been developed for 3D imaging of silicate-hosted magnetite inclusions down to the stable SD limit of 30 nm.

2. Silicate-hosted magnetite inclusions in plagioclase and pyroxene span a wide range of domain state behaviours, including SD, SV, MV, SW and MD.

3. In plagioclase, a dominant cluster of oblate SD particles is found with mixed uniaxial/multiaxial anisotropy and $M_{rs}/M_s = 0.7$. In pyroxene, SD particles are predominantly prolate with uniaxial anisotropy and $M_{rs}/M_s = 0.5$.

4. The range of hysteresis properties observed in just two $\sim 650 - 2300 \mu m^3$ volumes of pyroxene and plagioclase, span almost the entire range of common domain-state diagnostic plots. This indicates that bulk average hysteresis parameters cannot predict a unique domain state, even for the particle ensemble inside a single exsolved silicate crystal.

5. Because shape and size equally determine the hysteresis properties of natural magnetite inclusions, the Butler-Banerjee plot performs best in terms of domain-state diagnosis, despite failing to account for MV states.

6. The morphology of the magnetite inclusions highlights the need to extend Néel's SD theory in the context of single-crystal paleomagnetism towards SV and MV magnetization states, as these may be dominant carriers of stable paleomagnetic remanence in silicates.

References

Ahrens, J., B. Geveci, and C. Law (2005), *Paraview: An end-user tool for large data visualization. The visualization handbook*, 717 p. pp., Kiteware.

Argyle, K., and D. Dunlop (1984), Theoretical domain structure in multidomain magnetite particles, *Geophys. Res. Lett.*, *11*.

Austin, J., D. Hillan, P. Schmidt, and C. Foss (2014), Understanding magnetism in the Giles Complex, Musgrave Block, SA, *Preview*, *171*, 41–44.

Ayachit, U. (2015), *The ParaView Guide: A Parallel Visualization Application*, Kitware.

Beckwith, M. S., K. S. Beckwith, P. Sikorski, N. T. Skogaker, T. H. Flo, and Ø. Halaas (2015), Seeing a mycobacterium-infected cell in nanoscale 3d: correlative imaging by light microscopy and fib/sem tomography, *PLoS One*, *10*(9).

Brogden, V. (2015), Method and apparatus for slice and view sample imaging, uS Patent 9,218,940.

Butler, R. F., and S. K. Banerjee (1975), Theoretical single-domain grain size range in magnetite and titanomagnetite, *J. Geophys. Res.*, *80*, 4049 – 4058.

Cao, S., W. Tirry, W. Van Den Broek, and D. Schryvers (2009), Optimization of a fib/sem slice-and-view study of the 3d distribution of ni4ti3 precipitates in ni–ti, *Journal of microscopy*, *233*(1), 61–68.

Church, N. S., K. Fabian, and S. A. McEnroe (2016), Nonlinear Preisach maps: Detecting and characterizing separate remanent magnetic fractions in complex natural samples, *Journal of Geophysical Research-Solid Earth*, *121*(12), 8373–8395.

Cignoni, P., M. Callieri, M. Corsini, M. Dellepiane, F. Ganovelli, and G. Ranzuglia (2008), Meshlab: an open-source mesh processing tool., in *Eurographics Italian chapter conference*, vol. 2008, pp. 129–136.

Davis, K. E. J. E., and P. S. Letters (1981), Magnetite rods in plagioclase as the primary carrier of stable NRM in ocean floor gabbros., *Earth and Planetary Science Letters*, *55*(1), 190–198.

Day, R., M. Fuller, and V. A. Schmidt (1977), Hysteresis properties of titanomagnetites: grain-size and compositional dependence, *Phys.Earth Planet. Inter.*, *13*, 260–267.

Ding, R., and I. P. Jones (2011), An fib–sem slice-and-view study of three-dimensional beta phase distribution in ti–6al–4v, *Journal of electron microscopy*, *60*(2), 149–155.

Dunlop, D. (1973), Superparamagnetic and single-domain threshold sizes in magnetite, *J. Geophys. Res.*, *78*, 1780–1793.

Dunlop, D. (2002), Theory an application of the day plot (m_{rs}/m_s versus h_{cr}/h_c) 1. theoretical curves and tests using titanomagnetite data, *J. Geophys. Res.*, *107*, 1–22.

Dunlop, D. J., and M.-M. Bina (1977), The coercive force spectrum of magnetite at high temperatures: evidence for thermal activation below the blocking temperature, *Geophys. J. R. astr. Soc.*, *51*, 121–147.

Dunlop, D. J., and Ö. Özdemir (1997), *Rock magnetism: fundamentals and frontiers*, vol. 3, Cambridge university press.

Einsle, J. F., R. J. Harrison, T. Kasama, P. Ó. Conbhuí, K. Fabian, W. Williams, L. Woodland, R. R. Fu, B. P. Weiss, and P. A. Midgley (2016), Multi-scale three-dimensional characterization of iron particles in dusty olivine: Implications for paleomagnetism of chondritic meteorites, *American Mineralogist*, *101*(9), 2070–2084.

Enkin, R. J., and D. Dunlop (1987), A micromagnetic study of pseudo-single-domain remanence in magnetite, *J. Geophys. Res.*, *92*, 12,726–12,740.

Enkin, R. J., and W. Williams (1994), Three-dimensional micromagnetic analysis of stability in fine magnetic grains, *J. Geophys. Res.*, *99*, 611–618.

Fabian, K., and A. Hubert (1999), Shape-induced pseudo-single-domain remanence, *Geophysical Journal International*, *138*(3), 717–726.

Fabian, K., and V. P. Shcherbakov (2018), Energy barriers in three-dimensional micromagnetic models and the physics of thermoviscous magnetization, *Geophysical Journal International*, *215*(1), 314–324, doi:10.1093/gji/ggy285.

Fabian, K., A. Kirchner, W. Williams, F. Heider, T. Leibl, and A. Hubert (1996), Three-dimensional micromagnetic calculations for magnetite using FFT, *Geophys. J. Int.*, *124*, 89–104.

Fagerland, S. K. (2014), Investigation of focused ion beam/scanning electron microscope parameters for slice and view and energy dispersive x-ray spectroscopy of embedded brain tissue, Master's thesis, Institutt for fysikk.

Fang, Q., and D. A. Boas (2009), Tetrahedral mesh generation from volumetric binary and grayscale images, in *2009 IEEE International Symposium on Biomedical Imaging: From Nano to Macro*, IEEE, doi:10.1109/isbi.2009.5193259.

Feinberg, J. M., H.-R. Wenk, P. R. Renne, and G. R. Scott (2004), Epitaxial relationships of clinopyroxene-hosted magnetite determined using electron backscatter diffraction (ebsd) technique, *American Mineralogist*, *89*(2-3), 462–466.

Feinberg, J. M., G. R. Scott, P. R. Renne, and H.-R. Wenk (2005), Exsolved magnetite inclusions in silicates: Features determining their remanence behavior, *Geology*, *33*(6), 513, doi:10.1130/g21290.1.

Fleet, M., G. A. Bilcox, and R. L. Barnett (1980), Oriented magnetite inclusions in pyroxenes from the Grenville Province, *The Canadian Mineralogist*, *18*(1), 89–99.

Frandsen, C., S. Stipp, S. McEnroe, M. Madsen, and J. Knudsen (2004), Magnetic domain structures and stray fields of individual elongated magnetite grains revealed by magnetic force microscopy (MFM), *Physics of the Earth and Planetary Interiors*, *141*(2), 121–129, doi:10.1016/j.pepi.2003.12.001.

Guehrs, E., M. Schneider, C. M. Günther, P. Hessing, K. Heitz, D. Wittke, A. L.-S. Oliver, N. Jakubowski, J. Plendl, S. Eisebitt, et al. (2017), Quantification of silver nanoparticle uptake and distribution within individual human macrophages by fib/sem slice and view, *Journal of nanobiotechnology*, *15*(1), 21.

Harrison, R. J., X. Zhao, P. Hu, T. Sato, D. Heslop, A. R. Muxworthy, H. Oda, V. S. Kuppili, and A. P. Roberts (2019), Simulation of remanent, transient, and induced forc diagrams for interacting particles with uniaxial, cubic, and hexagonal anisotropy, *Journal of Geophysical Research: Solid Earth*, *124*(12), 12,404–12,429.

Hodych, J. (1990), Magnetic hysteresis as a function of low temperature in rocks: evidence for internal stress control of remanence in multi-domain and pseudo-single-domain magnetite, *Phys. Earth Planet. Inter.*, *64*(1), 21–36.

Hubert, A., and R. Schäfer (1998), *Magnetic Domains*, Springer, Berlin, Heidelberg, New York.

Joffe, I., and R. Heuberger (1974), Hysteresis properties of distributions of cubic single-domain ferromagnetic particles, *Phil. Mag.*, *29*, 1051–1059.

Khakhalova, E., B. M. Moskowitz, W. Williams, A. R. Biedermann, and P. Solheid (2018), Magnetic vortex states in small octahedral particles of intermediate titanomagnetite, *Geochemistry, Geophysics, Geosystems*, *19*(9), 3071–3083, doi:10.1029/2018gc007723.

Krása, D., C. D. W. Wilkinson, N. Gadegaard, X. Kong, H. Zhou, A. P. Roberts, A. R. Muxworthy, and W. Williams (2009), Nanofabrication of two-dimensional arrays of magnetite particles for fundamental rock magnetic studies, *Journal of Geophysical Research*, *114*(B2), doi:10.1029/2008jb006017.

Lappe, S.-C. L., J. M. Feinberg, A. Muxworthy, and R. J. Harrison (2013), Comparison and calibration of nonheating paleointensity methods: A case study using dusty olivine, *Geochemistry, Geophysics, Geosystems*, *14*(7), 2143–2158.

Lascu, I., R. J. Harrison, Y. Li, J. R. Muraszko, J. E. T. Channell, A. M. Piotrowski, and D. A. Hodell (2015), Magnetic unmixing of first-order reversal curve diagrams using principal component analysis, *Geochemistry, Geophysics, Geosystems*, *16*(9), 2900–2915, doi:10.1002/2015gc005909.

Maier, W., H. Howard, R. Smithies, S. Yang, S.-J. Barnes, H. O'Brien, H. Huhma, and S. Gardoll (2015), Magmatic ore deposits in mafic–ultramafic intrusions of the giles event, western australia, *Ore Geology Reviews*, *71*, 405–436, doi:10.1016/j.oregeorev.2015.06.010.

McEnroe, S., J. Skilbrei, P. Robinson, F. Heidelbach, F. Langenhorst, and L. Brown (2004), Magnetic anomalies, layered intrusions and mars, *Geophysical Research Letters*, *31*(19).

McNab, T. K., R. A. Fox, and A. J. F. Boyle (1968), Some magnetic properties of magnetite (Fe_3O_4) microcrystals, *J. Appl. Phys.*, *39*, 5703 – 5711.

Mulders, J. L., G. Knott, and B. Lich (2006), Dualbeam slice & view: Practical aspects for collecting 3d cortex image data, *Microscopy and Microanalysis*, *12*(S02), 1324–1325.

Muxworthy, A. R., and W. Williams (2006), Critical single-domain/multidomain grain sizes in noninteracting and interacting elongated magnetite particles: Implications for magnetosomes, *Journal of Geophysical Research: Solid Earth*, *111*(B12).

Muxworthy, A. R., and W. Williams (2008), Critical superparamagnetic/single-domain grain sizes in interacting magnetite particles: implications for magnetosome crystals, *Journal of The Royal Society Interface*, *6*(41), 1207–1212, doi:10.1098/rsif.2008.0462.

Nagy, L., W. Williams, L. Tauxe, and A. R. Muxworthy (2019), From nano to micro: Evolution of magnetic domain structures in multidomain magnetite, *Geochemistry, Geophysics, Geosystems*, *20*(6), 2907–2918.

Néel, L. (1955), Some theoretical aspects of rock-magnetism, *Adv. Phys.*, *4*, 191–243.

Ó Conbhuí, P., W. Williams, K. Fabian, P. Ridley, L. Nagy, and A. R. Muxworthy (2018), MERRILL: Micromagnetic Earth related robust interpreted language laboratory, *Geochemistry, Geophysics, Geosystems*, *19*, doi:10.1002/2017gc007279.

Parry, L. (1982), Magnetization of immobilized particle dispersions with two distinct particle sizes, *Physics of the Earth and Planetary interiors*, *28*(3), 230–241.

Rave, W., K. Fabian, and A. Hubert (1998a), Magnetic states of small cubic particles with uniaxial anisotropy, *J. Magn. Magn. Mater.*, *190*, 332–348.

Rave, W., K. Ramstöck, and A. Hubert (1998b), Corners and nucleation in micromagnetics, *J. Magn. Magn. Mater.*, *183*, 329–333.

Renne, P. R., G. R. Scott, J. M. G. Glen, and J. M. Feinberg (2002), Oriented inclusions of magnetite in clinopyroxene: Source of stable remanent magnetization in gabbros of the messum complex, namibia, *Geochemistry, Geophysics, Geosystems*, *3*(12), 1–11, doi: 10.1029/2002gc000319.

Roberts, A. P., L. Tauxe, D. Heslop, X. Zhao, and Z. Jiang (2018), A critical appraisal of the "Day" diagram, *Journal of Geophysical Research: Solid Earth*, *123*(4), 2618–2644, doi: 10.1002/2017jb015247.

Robinson, P., S. A. McEnroe, N. Miyajima, K. Fabian, and N. Church (2016), Remanent magnetization, magnetic coupling, and interface ionic configurations of intergrown rhombohedral and cubic Fe-Ti oxides: A short survey, *American Mineralogist*, *101*(3-4), 518–530.

Schmidt, R., and K. Singh (2010), Meshmixer: an interface for rapid mesh composition, in *ACM SIGGRAPH 2010 Talks*, pp. 1–1.

Soffel, H. C. (1977), Domain structure of titanomagnetites and its variation with temperature, *J. Geomag. Geoelectr.*, *29*, 277–284.

Stacey, F. D. (1961), Theory of magnetic properties of igneous rocks in alternating fields, *Phil. Mag.*, *6*, 1241–1260.

Stacey, F. D., and S. K. Banerjee (1974), *The physical principles of rock magnetism*, Elsevier, Amsterdam.

Tarduno, J. A., R. D. Cottrell, R. K. Bono, H. Oda, W. J. Davis, M. Fayek, O. van't Erve, F. Nimmo, W. Huang, E. R. Thern, et al. (2020), Paleomagnetism indicates that primary magnetite in zircon records a strong hadean geodynamo, *Proceedings of the National Academy of Sciences*, *117*(5), 2309–2318.

Tauxe, L., H. N. Bertram, and C. Seberino (2002), Physical interpretation of hysteresis loops: Micromagnetic modeling of fine particle magnetite, *Geochemistry Geophysics Geosystems*, *3*, art. no.–1055.

ter Maat, G. W., K. Fabian, N. S. Church, and S. A. McEnroe (2020), Separating geometry-from stress-induced remanent magnetization in magnetite with ilmenite lamellae from the Stardalur basalts, Iceland, *Geochemistry, Geophysics, Geosystems*, *21*, doi: 10.1029/2019gc008761.

Tseng, Q., I. Wang, E. Duchemin-Pelletier, A. Azioune, N. Carpi, J. Gao, O. Filhol, M. Piel, M. Théry, and M. Balland (2011), A new micropatterning method of soft substrates reveals that different tumorigenic signals can promote or reduce cell contraction levels, *Lab Chip*, *11*, 2231–2240, doi:10.1039/C0LC00641F.

Usui, Y., T. Shibuya, Y. Sawaki, and T. Komiya (2015), Rock magnetism of tiny exsolved magnetite in plagioclase from a Paleoarchean granitoid in the Pilbara craton, *Geochemistry, Geophysics, Geosystems*, *16*(1), 112–125, doi:10.1002/2014gc005508.

Warr, L. N., J. Wojatschke, B. M. Carpenter, C. Marone, A. M. Schleicher, and B. A. van der Pluijm (2014), A "slice-and-view"(fib–sem) study of clay gouge from the safod creeping section of the san andreas fault at 2.7 km depth, *Journal of Structural Geology*, *69*, 234–244.

Wenk, H.-R., K. Chen, and R. Smith (2011), Morphology and microstructure of magnetite and ilmenite inclusions in plagioclase from adirondack anorthositic gneiss, *American Mineralogist*, *96*(8-9), 1316–1324.

Witt, A., K. Fabian, and U. Bleil (2005), Three-dimensional micromagnetic calculations for naturally shaped magnetite: Octahedra and magnetosomes, *Earth and Planetary Science Letters*, *233*(3-4), 311–324.

A:

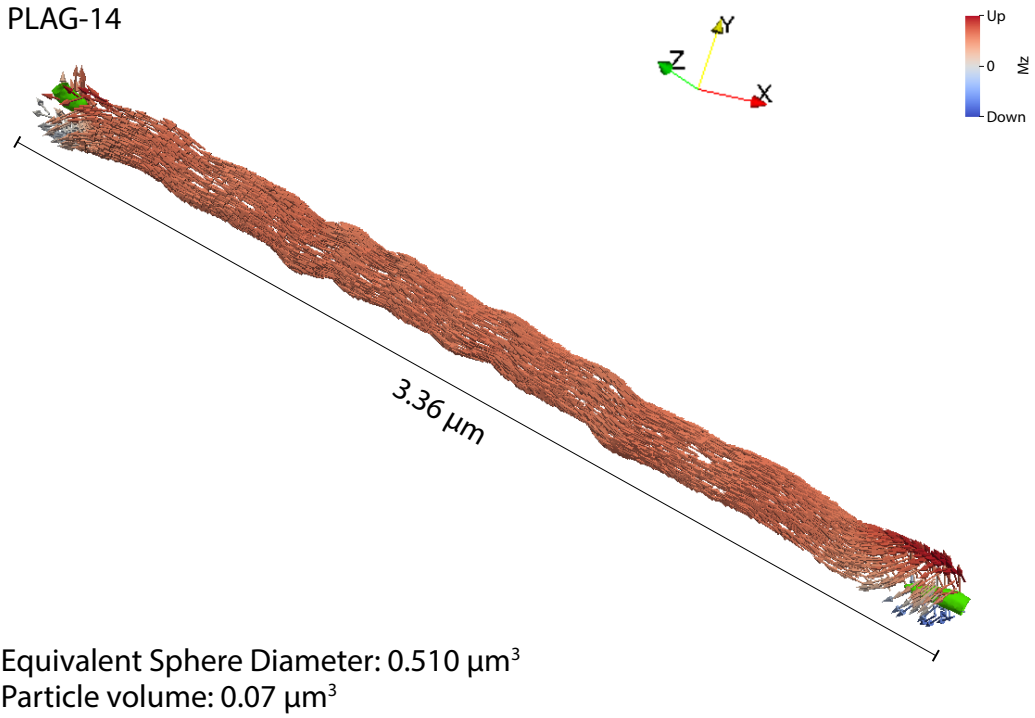

Figure A.1. Magnetic model of a 3.36 μm long magnetite needle in plagioclase, minimized in zero-field.

Acknowledgments

The FIB-SEM and Slice-and-View work was preformed at the NTNU Nanolab and the Norwegian infrastructure for micro- and nanofabrication as part of a PhD-project funded by NTNU. The Research Council of Norway is acknowledged for the support to the Norwegian Micro-and Nano-Fabrication Facility, NorFab, Project 245963/F50. The calculations and usage of a Linux server was possible with granted access by IGP and a designated workstation with remote access. We thank Phil Schmidt for providing these very interesting samples. We also wish to thank Lesleis Nagy and Thomas Berndt for their detailed and constructive reviews. Particle meshes for replication of results and appendix figures can be found at the online repository dataverse.no (https://doi.org/10.18710/Q0F8PA).

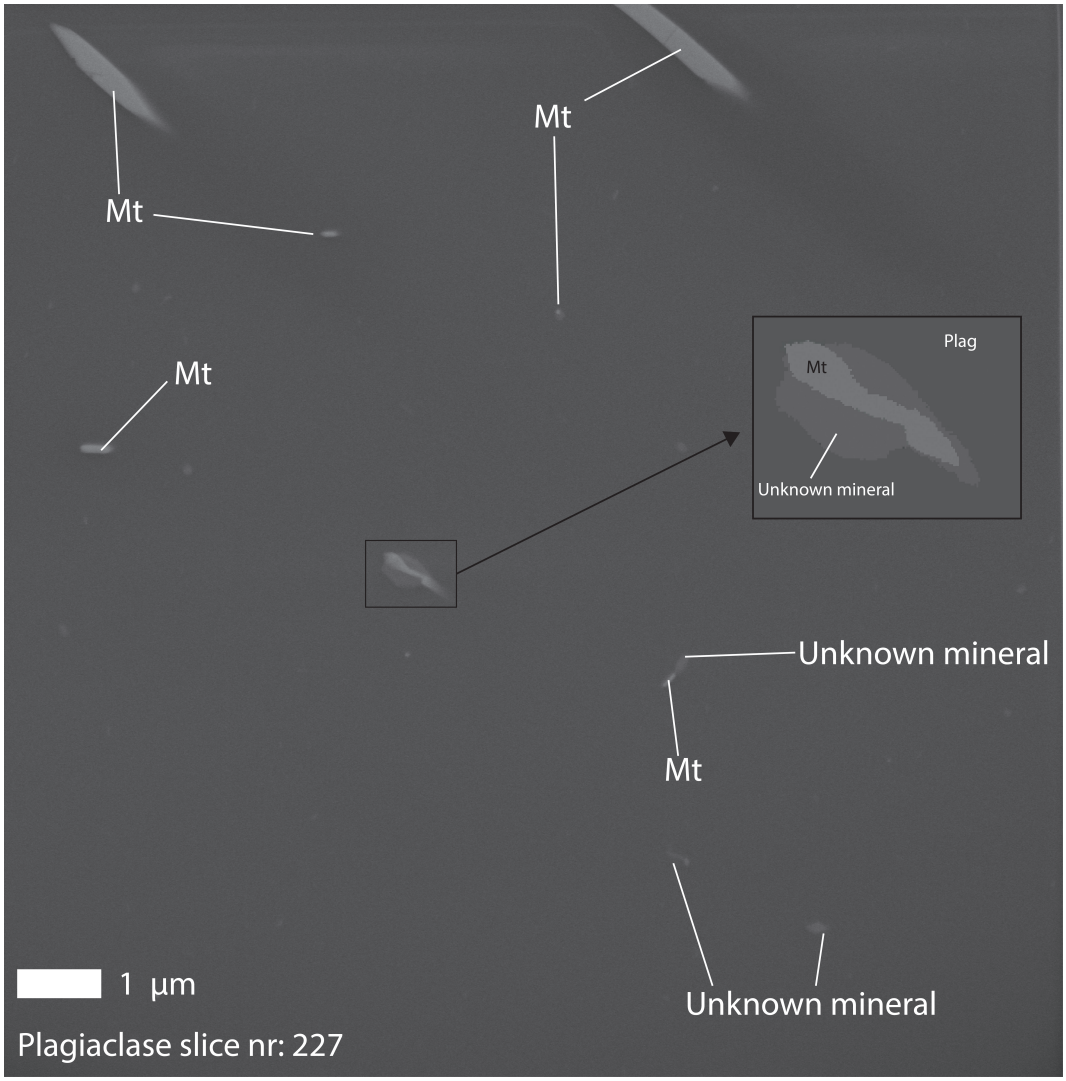

852 **Figure A.2.** Image of slice 227 in plagioclase showing mainly magnetite associated with an unknown
853 mineral that often occurs at an edge or coated around the magnetite.

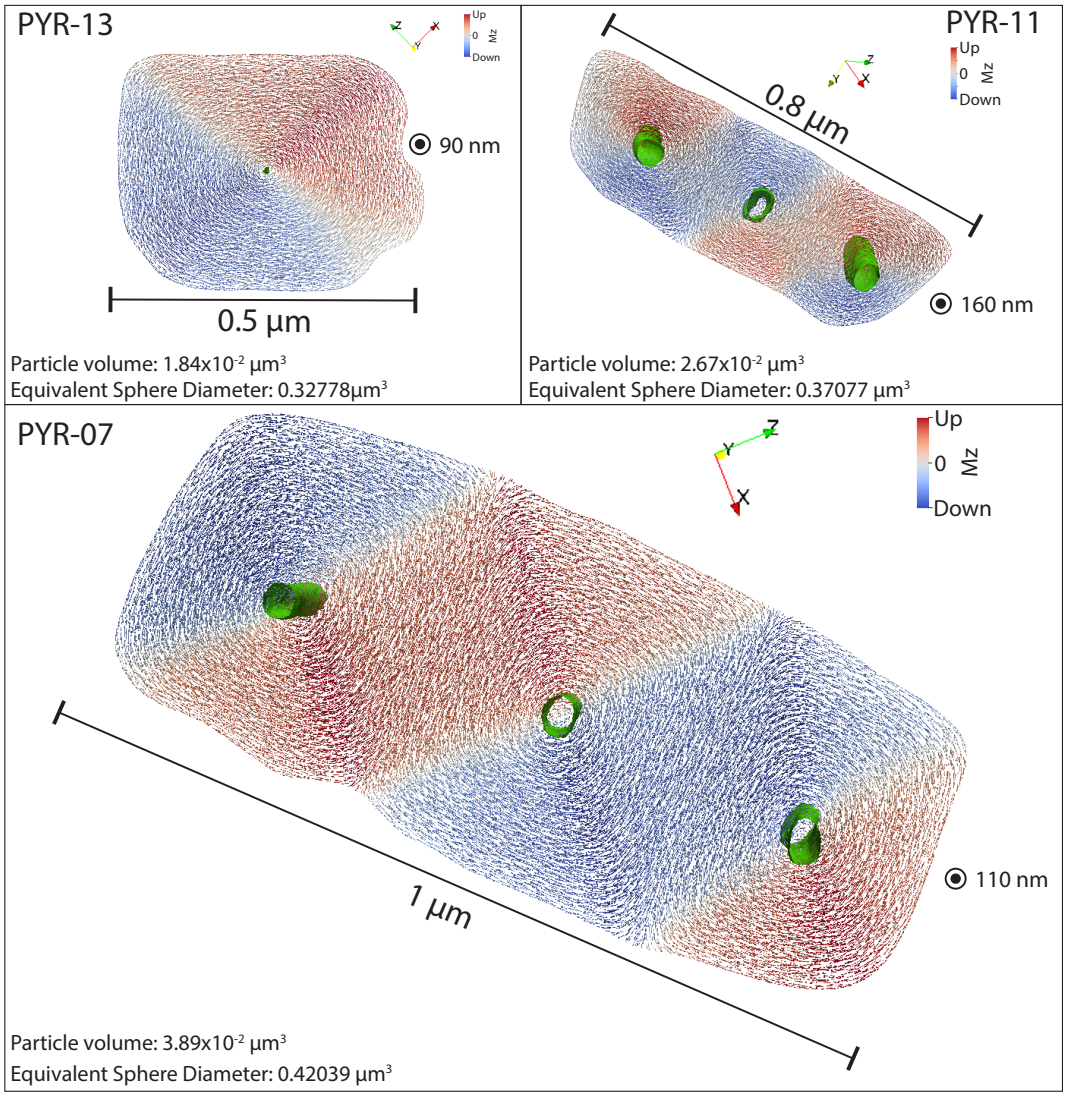

854 **Figure A.3.** Rendering of the zero-field minimization of large particles labeled as SW.

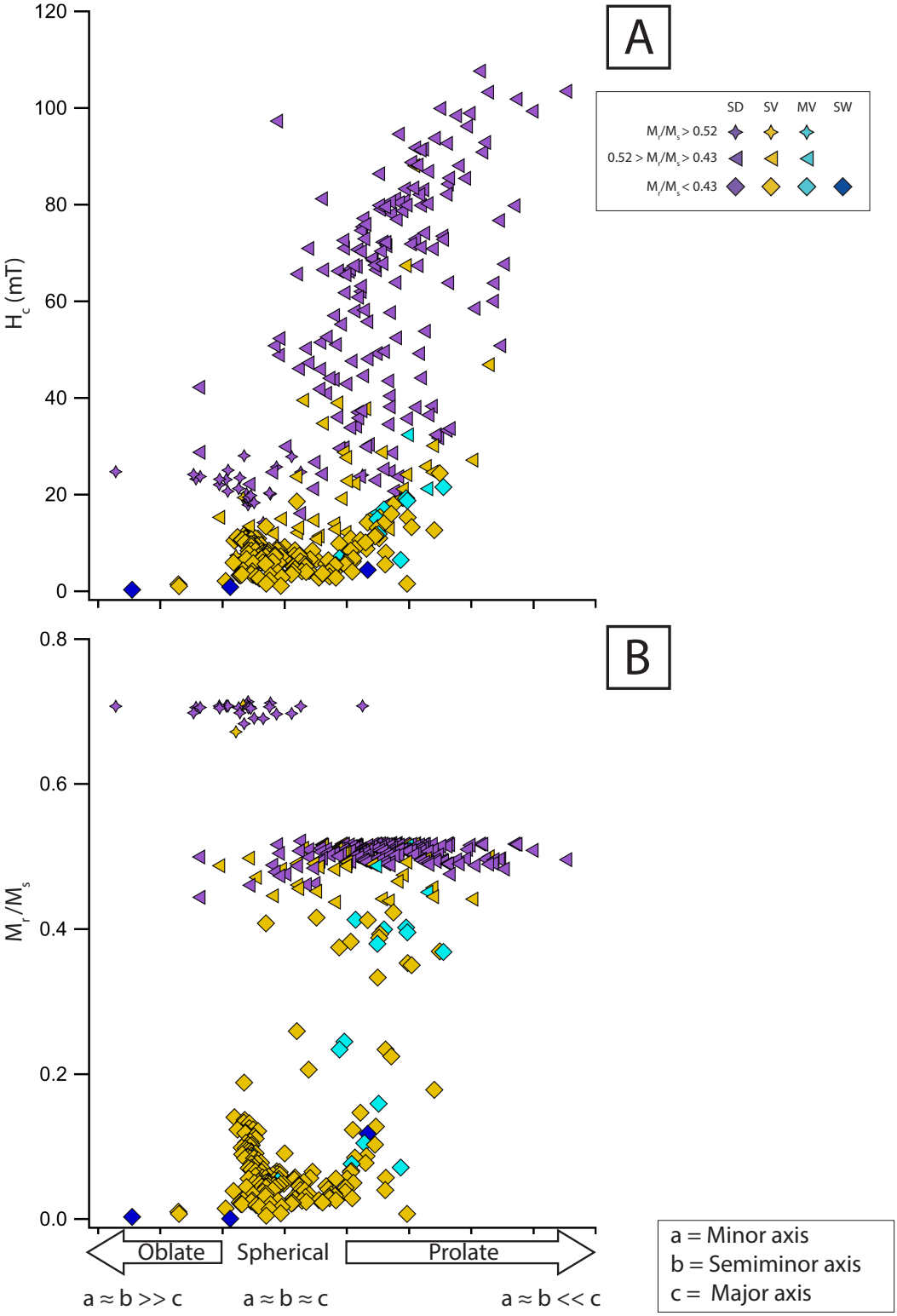

855 **Figure A.4.** a) Coercivity, H_c and b) remanence ratio, M_{rs}/M_s as a function of particle prolate-
856 ness/oblateness.

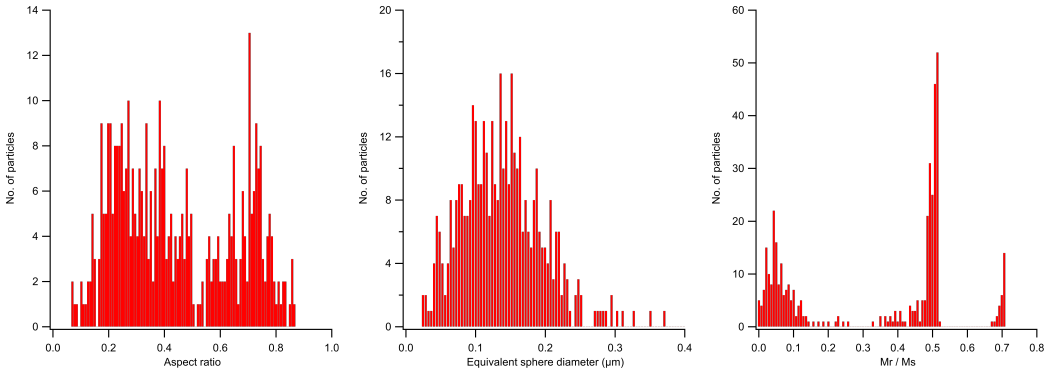

Figure A.5. Histograms showing the particle distribution of M_r/M_{rs}, Aspect ratio and Equivalent sphere diameter.

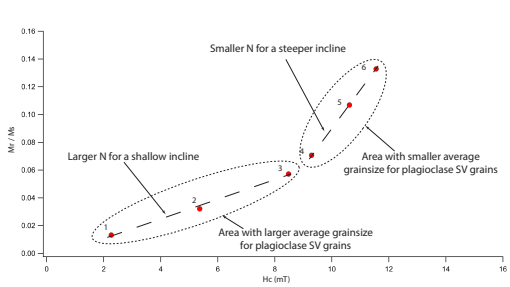

Particle	Hc (mT)	Mr (Am²)	Mr / Ms	Demagnitization factor (N)	Equivalent sphere volume diameter (µm)	aspect ratio
1:	5,37	1,83E-16	3,21E-02	0,26	0,277	0,49
2:	2,27	6.76E-17	1.32E-02	0,28	0,273	0,56
3:	8,48	1,34E-16	5,72E-02	0,25	0,210	0,86
4:	9,29	3,99E-17	7,07E-02	0,22	0,131	0,71
5:	10,62	3,08E-17	1,07E-01	0,16	0,105	0,66
6:	11,55	3,36E-17	1,33E-01	0,14	0,100	0,70

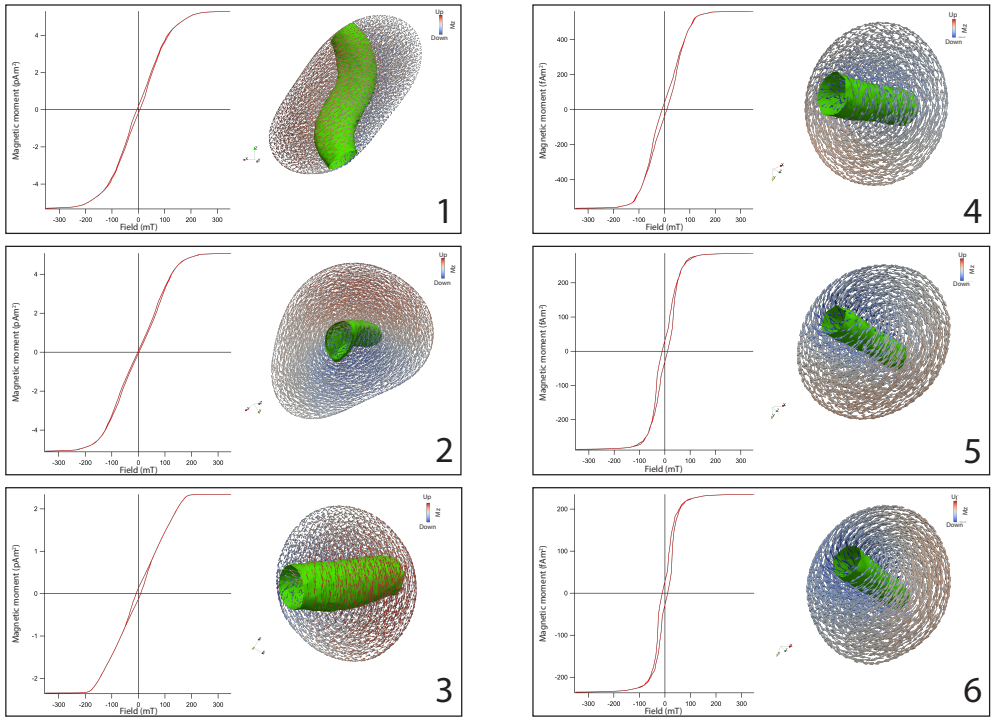

Figure A.6. Showing a selection of six particles that represents the two different slopes observed among SV plagioclase particles. N was calculated and volume corrected from the slope between M_r and H_c. The dotted ellipses shoving the clusters of similar particle sizes that differs in the two trends.